Finite difference technique for the evaluation of the transverse displacements in force-based beam finite elements

Paolo Di Re *, Daniel Macabeo Benaim Sanchez

Department of Structural and Geotechnical Engineering, Sapienza University of Rome, Via Eudossiana 18, 00184 Rome, Italy

ARTICLE INFO

ABSTRACT

In force-based beam finite elements, cross-section transverse displacements are often needed for post-processing purposes and for geometrically nonlinear structural analysis. This involves the complex integration of the cross-section strains along the beam axis, typically done by the Curvature and Shear Based Displacement Interpolation (CSBDI) technique. Although, the CSBDI is sufficiently accurate for standard applications, this may cause numerical issues when many quadrature cross-sections are placed along the element length. This work presents a novel technique for computing the transverse displacements of a 3D Timoshenko beam, based on a finite difference approximation of the bending and shear compatibility conditions, which avoids the issues of the CSBDI. The proposed technique is introduced in a force-based finite element formulation with moderately large deformations, endowed with a corotational approach, suitable for analyzing geometrically nonlinear framed structures. Detailed investigation of the accuracy and efficiency of the proposed technique is conducted comparing its performance with that of the CSBDI approach.

1. Introduction

Simulating the mechanical response of framed structures is often required in many engineering fields. These structures can be subjected to various loading conditions, such as wind, earthquake, impact, or explosion, that can easily produce severe level of deformations. Hence, the mechanical modeling of frames is a challenging task, as they can undergo complex geometric nonlinearities that usually affect the stiffness, strength, ductility, and energy dissipation capacity of the structure and interact with plasticity and damage mechanisms, leading to uncertain or unstable responses.

In recent decades, several enhanced beam models have been proposed for the analysis of frame structures under geometric nonlinearities, e.g. [1–5], based on various approaches, such as analytical methods or finite element (FE) analysis. A comprehensive review is reported in [6,7], starting from the first proposals in [8–10]. Additional earlier works that are worth to be mentioned are those by Silveira et al. [11] and Schulz et al. [12]. The former compared six beam formulations based either on the updated or the total Lagrangian formulation, i.e., the geometrically exact Euler–Bernoulli model by Alves [13], the two Euler–Bernoulli models by Yang and Kuo [14], one considering the natural deformation approach and the other the external stiffness approach, and the three Euler–Bernoulli and Timoshenko models by Pacoste and Eriksson [15]. A nonlinear Timoshenko beam model based on the total Lagrangian approach has also been proposed by Schulz et al. [12] where cross-section rotations are computed by interpolating and integrating the bending curvatures along the element axis. They also presented a detailed review of the first works on geometrically nonlinear Timoshenko beams, such as [8,16,17].

---

* Corresponding author.
 E-mail addresses: paolo.dire@uniroma1.it (P. Di Re), benaimsanchez.1920748@studenti.uniroma1.it (D.M. Benaim Sanchez).

More recent approaches have also been proposed. For instance, Jirasek et al. [18] introduced a two-dimensional (2D) Euler–Bernoulli beam model with elastic material but based on an exact definition of geometric nonlinearities. They use a finite difference approach to determine the numerical solution of the governing equations that are consistently derived in the exact element deformed configuration.

However, beam FE models based on corotational approaches [19–22] have been largely preferred. These allow the decoupling of the rigid body motions of the element, treated under the assumption of large displacement, from the deformation displacements, which allows the adoption of constitutive relationships formulated under the hypothesis of small deformations [6,23–25].

In this framework, the adoption of force-based element formulations was shown to be much more efficient than classical displacement-based ones [26–32]. Force-based formulations rely on the interpolation of the internal forces according to the element equilibrium, which is satisfied in strong form along the axis. These are advantageous for geometrically linear analysis as they can model each structural member with a single beam FE and avoid shear locking problems. They also perform very well for geometrically nonlinear simulations, although displacement-based formulations are sometimes preferred in this case (e.g., [33]), as the displacement interpolation permits an easier definition of the nonlinear compatibility conditions.

If the nonlinearities are captured by the corotational approach and the intra-element deformations are assumed to be small, a single element per member is not enough to obtain accurate solutions. Neuenhofer and Filippou in 1998 [34] addressed this limitation by proposing an enhanced force-based beam model that removes the assumption of small deformations and includes the main nonlinear terms. They consider the linear elastic 2D Euler–Bernoulli beam theory and determine the interpolation of the internal forces by enforcing the element equilibrium in the deformed configuration, i.e., by accounting for the transverse cross-section displacements. The element governing equations are derived on the basis of the Hellinger–Reissner variational principle. Although transverse cross-section displacements are considered large, cross-section rotations are still assumed to be small and the nonlinear influence of shear forces on axial stress is neglected, thus accounting only for moderately large deformations, based on the Von Karman theory [35,36]. Similarly, at the global level, a simpler P-Delta formulation is used instead of a corotational approach.

An innovative numerical procedure is proposed to compute the transverse displacements of the quadrature cross-sections. This is based on the interpolation and double integration of the bending curvatures along the element axis and is named Curvature Based Displacement Interpolation (CBDI).

De Souza [6] generalized the model by Neuenhofer and Filippou and the CBDI technique to the case of three-dimensional (3D) Euler–Bernoulli elements and applied a corotational formulation to account for large nodal displacements for both 2D and 3D models. He also incorporated the material nonlinearities and proposed an efficient algorithm to determine the element state during the classic Newton–Raphson iterative solution scheme. Furthermore, he discusses the symmetry of the element flexibility matrix and the implications of neglecting the higher nonlinear geometric terms.

Sivaselvan et al. [37] presented a richer but more complex element formulation for 2D Euler–Bernoulli elements based on fully large deformation assumption and a mixed approach. Indeed, they claim that the CBDI technique results in oscillatory displacement fields when many quadrature cross-sections are used along the element and/or when very large deformations occur, and suggest to directly interpolate the cross-section displacements and rotations from the nodal degrees of freedom (DOFs). Indeed, other recent proposals also embrace a mixed formulation in which displacements are independently interpolated from the stresses [38–40]. This approach circumvents the need to compute the displacements from the strains, as required by the equilibrium conditions. Notably, these alternative methods yield even greater generality and accuracy compared to the force-based model proposed in [6], while maintaining similar or superior computational efficiency.

Regardless of the mixed formulation alternatives and the oscillatory problem of the CBDI technique, the work by Jafari et al. [41] extended the 2D model by De Souza and the 2D CBDI technique to the analysis of curved elements. A following work by the same authors [42] addressed the case of Timoshenko beams by adding the interpolation of the shear strains along the element axis to that of the bending curvatures, thus resulting in the Curvature and Shear Based Displacement Interpolation (CSBDI) technique. They presented the model for linear elastic material analysis and Scott and Jafari [43] formalized the derivation for the case of nonlinear materials. The CSBDI was finally extended to the more general 3D Timoshenko elements by Rezaiee-Pajand and Gharaei-Moghaddam [44].

Recently, the model in [42] has also been adopted by Feng et al. [45] for the analysis of damaging structures, with the introduction of the nonlocal integral approach, and by Scott and Denavit [46] for the analysis of buckling effects in compressed elements. Moreover, the work in [47] has extended the model by Rezaiee-Pajand and Gharaei-Moghaddam [44] to include the contribution of rigid offsets placed at the end of the elements.

Although numerous formulations already exist in the literature with higher performances [38–40], the models in [42,44] are still very widely used for both research and professional applications and are, thus, the focus of this work. The robustness of the CBDI/CSBDI technique is investigated for constitutive linear and nonlinear applications, also showing that, when many quadrature cross-sections are required along the element, the matrices linking the cross-section transverse displacements to the bending curvatures and shear strains become ill-conditioned. Therefore, an alternative novel approach is proposed that avoids the issues of the CBDI/CSBDI. This relies on a finite difference (FD) integration of the beam bending/shear compatibility conditions and, thus, is named Finite Difference Displacement Integration (FDDI). Specifically, the FDDI technique exploits the location of the quadrature cross-sections to construct an FD approximation of the second order derivative of the transverse displacements. Thus, it integrates these displacements by properly imposing the boundary conditions and inverting the coefficient matrices that result from the FD approximation. The relationship between transverse displacements and bending curvatures/shear strains is expressed in a matrix form identical to that of the CBDI/CSBDI, which allows to formally keep unchanged and use the same definition of the element governing equations and solution algorithm of the models in [6,34,42,44].
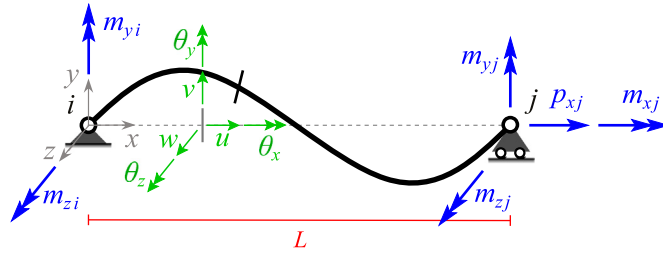
Fig. 1. Element local reference system: cross-section generalized displacements and element basic nodal forces.

The description is presented by referring to the more general case of a 3D Timoshenko beam, i.e., by considering the FE formulation by Rezaiee-Pajand and Gharaei-Moghaddam [44]. To handle the large displacements and rotations of the element nodes, the corotational formulation in [48] is used. This is based on the original proposal in [49] which considers additive quaternions to measure the nodal rotations in the global reference system. Moreover, the nonlinear coupling between the axial and torsional components, i.e., the Wagner terms, is included. For brevity, the corotational formulation is not described in this work and the reader can refer to [47,48] to further details.

In this work, both the linear elastic and nonlinear material cases are considered. For the element state solution algorithm required to ensure the compatibility conditions, although various proposals are reported in [6,34,42,44,45], that in [6] is used, which appears to be more stable and efficient.

It is important to note that the proposed technique extends beyond its application to the adopted geometrically nonlinear beam formulation. It can also be effectively employed for post-processing evaluations of transverse displacements in force-based beams operating under linear geometry, which is a prevalent standard in frame numerical analysis. Indeed, preliminary analyses are conducted on a simply supported beam under linear geometry, to further assess the performance of the CSBDI technique, and, more importantly, to study the accuracy of the FDDI technique in determining the general FE transverse displacements. Then, numerical applications are performed on paradigmatic geometrically nonlinear structures under linear and nonlinear material response.

The paper is organized as follows. First, the formulation of the 3D Timoshenko beam FE model with moderately large deformations is reviewed. Then, the CSBDI and FDDI techniques are described in a unified formulation. For the former, the ill-conditioning of the fundamental matrices is studied, while specific but fundamental computational schemes are shown for the latter. Finally, the numerical simulations are presented.

2. Beam element formulation

The following sections review the element formulation, starting with the main assumptions for the cross-section mechanics and then presenting the element governing equations.

2.1. Cross-section mechanics

The element formulation is based on the Timoshenko beam theory, which accounts for the transverse shear deformation. The beam element has two nodes i and j. The local coordinate system $(i; x, y, z)$ is defined such that the x axis coincides with the beam axis and y and z define the orthogonal cross-section plane (Fig. 1).

Under exact nonlinear kinematics and assuming rigid cross-section, the displacement fields of any point m of the beam, $\mathbf{u}_m(x, y, z) = \left\{ u_m(x, y, z) \quad v_m(x, y, z) \quad w_m(x, y, z) \right\}^T$, are nonlinear functions of the generalized cross-section displacements [40,50, 51], i.e. the rigid translations $u(x)$, $v(x)$ and $w(x)$, and rotations $\theta_x(x)$, $\theta_y(x)$ and $\theta_z(x)$ (Fig. 1).

The same rigid cross-section assumption gives rise to null in-plane strains, that is, $\varepsilon_{yy}(x, y, z) = \varepsilon_{zz}(x, y, z) = \gamma_{yz}(x, y, z) = 0$, and thus the non-null Green–Lagrange material strains at the point m are:

$$\boldsymbol{\varepsilon}_m(x, y, z) = \begin{Bmatrix} \varepsilon_{xx}(x, y, z) \\ \gamma_{xy}(x, y, z) \\ \gamma_{xz}(x, y, z) \end{Bmatrix} = \begin{Bmatrix} \frac{du_m(x,y,z)}{dx} + \frac{1}{2}\left[\frac{du_m(x,y,z)}{dx}\right]^2 + \frac{1}{2}\left[\frac{dv_m(x,y,z)}{dx}\right]^2 + \frac{1}{2}\left[\frac{dw_m(x,y,z)}{dx}\right]^2 \\ \frac{du_m(x,y,z)}{dy} + \frac{dv_m(x,y,z)}{dx} + \frac{du_m(x,y,z)}{dx}\frac{du_m(x,y,z)}{dy} + \frac{dv_m(x,y,z)}{dx}\frac{dv_m(x,y,z)}{dy} + \frac{dw_m(x,y,z)}{dx}\frac{dw_m(x,y,z)}{dy} \\ \frac{du_m(x,y,z)}{dz} + \frac{dw_m(x,y,z)}{dx} + \frac{du_m(x,y,z)}{dx}\frac{du_m(x,y,z)}{dz} + \frac{dv_m(x,y,z)}{dx}\frac{dv_m(x,y,z)}{dz} + \frac{dw_m(x,y,z)}{dx}\frac{dw_m(x,y,z)}{dz} \end{Bmatrix} \tag{1}$$

However, based on the Von Karman theory [35,36], cross-section rigid translations with respect to the reference axis are assumed as large but rotations are considered as small. Hence, displacements $\mathbf{u}_m(x, y, z)$ are linearized [6,44] obtaining:

$$\mathbf{u}_m(x, y, z) = \begin{Bmatrix} u_m(x, y, z) \\ v_m(x, y, z) \\ w_m(x, y, z) \end{Bmatrix} = \begin{Bmatrix} u(x) - y\theta_z(x) + z\theta_y(x) \\ v(x) - z\theta_x(x) \\ w(x) + y\theta_x(x) \end{Bmatrix} \tag{2}$$

Similarly, term $\frac{1}{2}\left[\frac{du_m(x,y,z)}{dx}\right]^2$ is neglected in the definition of the material strain $\varepsilon_{xx}(x,y,z)$, together with higher-order terms in the definition of $\gamma_{xy}(x,y,z)$ and $\gamma_{xz}(x,y,z)$, giving rise to a description of *moderately large deformation* [6,34,44]. By introducing Eq. (2) into Eq. (1), the material strains are re-written in terms of generalized cross-section displacements. Moreover, based on the previous assumption, the terms associated to $\left[\frac{d\theta_x(x)}{dx}\right]^2$, i.e., the Wagner terms related to geometric nonlinear torsion [24,48,52], are also neglected, and it results:

$$\boldsymbol{\varepsilon}_m(x,y,z) = \left\{ \begin{array}{c} \frac{du(x)}{dx} - y\frac{d\theta_z(x)}{dx} + z\frac{d\theta_y(x)}{dx} + \frac{1}{2}\left[\frac{dv(x)}{dx}\right]^2 + \frac{1}{2}\left[\frac{dw(x)}{dx}\right]^2 \\ -\theta_z(x) + \frac{dv(x)}{dx} - z\frac{d\theta_x(x)}{dx} \\ \theta_y(x) + \frac{dw(x)}{dx} + y\frac{d\theta_x(x)}{dx} \end{array} \right\} \tag{3}$$

To be noted is that, the Wagner term is accounted for in approximate way through the corotational formulation adopted to describe the large nodal displacement and rotations, as described in [47,48].

Eq. (3) is written in compact form, by introducing the compatibility matrix $\mathbf{a}_s(y,z)$:

$$\mathbf{a}_s(y,z) = \begin{bmatrix} 1 & -y & 0 & 0 & z & 0 \\ 0 & 0 & \sqrt{\psi_y} & -z\sqrt{\psi_x} & 0 & 0 \\ 0 & 0 & 0 & y\sqrt{\psi_x} & 0 & \sqrt{\psi_z} \end{bmatrix} \tag{4}$$

This relates $\boldsymbol{\varepsilon}_m(x,y,z)$ to the generalized cross-section strains $\mathbf{e}(x)$, that is the axial strain $\varepsilon_G(x)$, flexural curvatures $\chi_z(x)$ and $\chi_y(x)$, torsional curvature $\chi_x(x)$, and shear strains $\gamma_y(x)$ and $\gamma_z(x)$. The expression results as:

$$\boldsymbol{\varepsilon}_m(x,y,z) = \mathbf{a}_s(y,z)\,\mathbf{e}(x) \tag{5}$$

with:

$$\mathbf{e}(x) = \left\{ \begin{array}{c} \varepsilon_G(x) \\ \chi_z(x) \\ \gamma_y(x) \\ \chi_x(x) \\ \chi_y(x) \\ \gamma_z(x) \end{array} \right\} = \left\{ \begin{array}{c} u'(x) + \frac{1}{2}\left[v'(x)\right]^2 + \frac{1}{2}\left[w'(x)\right]^2 \\ \theta_z'(x) \\ v'(x) - \theta_z(x) \\ \theta_x'(x) \\ \theta_y'(x) \\ w'(x) + \theta_y(x) \end{array} \right\} \tag{6}$$

where prime symbol indicates the derivative with respect to x. The kinematic matrix $\mathbf{a}_s(x)$ in Eq. (4) is properly defined with the introduction of the torsional ψ_x, and shear ψ_y and ψ_z correction coefficients, to account for torsional and shear warping in an approximate way [4]. The corrections presented herein are based on the linear elastic solutions for beams subjected to shear and torsion. In this study, the same definition of $\mathbf{a}_s(x)$ is adopted also in the elasto-plastic range, as it provides the simplest yet reasonable description of the cross-section kinematics.

The work-conjugate stresses at point m are $\boldsymbol{\sigma}_m(x,y,z) = \left\{ \sigma_{xx}(x,y,z) \quad \tau_{xy}(x,y,z) \quad \tau_{xz}(x,y,z) \right\}^T$. Thus, standing on the virtual work principle, the generalized cross-section stresses (internal forces) result as:

$$\mathbf{s}(x) = \left\{ N(x) \quad M_z(x) \quad T_y(x) \quad M_x(x) \quad M_y(x) \quad T_z(x) \right\}^T = \int_A \mathbf{a}_s^T(y,z)\,\boldsymbol{\sigma}_m(x,y,z)\,dA \tag{7}$$

where vector $\mathbf{s}(x)$ collects the normal force $N(x)$, bending moments $M_z(x)$ and $M_y(x)$, torsional moment $M_x(x)$, and shear forces $T_y(x)$ and $T_z(x)$.

Finally, the cross-section stiffness matrix $\mathbf{k}_s(x)$ is given by:

$$\mathbf{k}_s(x) = \int_A \mathbf{a}_s^T(y,z)\,\mathbf{k}_m(x,y,z)\,\mathbf{a}_s(y,z)\,dA \tag{8}$$

being A the cross-section area. This matrix governs the incremental cross-section generalized stress–strain relationship, i.e. $\delta\mathbf{s}(x) = \mathbf{k}_s(x)\,\delta\mathbf{e}(x)$, being $\mathbf{k}_m(x,y,z)$ the material stiffness matrix governing the incremental material stress–strain relationship, that is $\delta\boldsymbol{\sigma}_m(x,y,z) = \mathbf{k}_m(x,y,z)\,\delta\boldsymbol{\varepsilon}_m(x,y,z)$.

It is worth to show that, for a linear elastic isotropic material, the material stiffness matrix is diagonal, $\mathbf{k}_m(x,y,z) = \text{diag}\{E,G,G\}$, depending on the Young's and shear moduli, E and G. Hence, for a homogeneous cross-section, the stiffness matrix $\mathbf{k}_s(x)$ results as:

$$\mathbf{k}_s(x)^{LE} = \begin{bmatrix} EA & -ES_z & 0 & 0 & ES_y & 0 \\ -ES_z & EI_z & 0 & 0 & -EI_{yz} & 0 \\ 0 & 0 & G\psi_y A & -G\sqrt{\psi_y\psi_x}S_y & 0 & 0 \\ 0 & 0 & -G\sqrt{\psi_y\psi_x}S_y & G\psi_x I_\rho & 0 & G\sqrt{\psi_z\psi_x}S_z \\ ES_y & -EI_{yz} & 0 & 0 & EI_y & 0 \\ 0 & 0 & 0 & G\sqrt{\psi_z\psi_x}S_z & 0 & G\psi_z A \end{bmatrix} \tag{9}$$

where $\{S_y;\ S_z\}$, $\{I_z;\ I_y;\ I_{yz}\}$ and I_ρ denote the first, the second and the polar moments of area of the cross-section, respectively. The products $A_y^* = \psi_y A$, $A_z^* = \psi_z A$ and $J = \psi_x I_\rho$ define the shear areas A_y^* and A_z^* and torsional inertia J, respectively.

It is observed that, if axes y and z are principal axes, all non-diagonal term vanish, and the cross-section stiffness matrix assumes the simpler form $\mathbf{k}_s(x) = \mathrm{diag}\left\{EA, EI_z, GA_y^*, GJ, EI_y, GA_z^*\right\}$, i.e. absence of coupling between the generalized section components.

2.2. Element mechanics

In the element local reference system, the rigid body motions are removed and the element formulation is derived referring to the six basic deformation displacements $\mathbf{v}$ and the work-conjugate basic nodal forces $\mathbf{q}$ (Fig. 1), i.e.:

$$\mathbf{v} = \left\{u_{xj}\quad \theta_{zi}\quad \theta_{zj}\quad \theta_{xj}\quad \theta_{yi}\quad \theta_{yj}\right\}^T \qquad \text{and} \qquad \mathbf{q} = \left\{p_{xj}\quad m_{zi}\quad m_{zj}\quad m_{xj}\quad m_{yi}\quad m_{yj}\right\}^T \tag{10}$$

The formulation is based on an equilibrated approach, where the cross-section stresses $\mathbf{s}(x)$ are interpolated from the nodal forces $\mathbf{q}$, by imposing the equilibrium in the deformed configuration [6], i.e. by considering the transverse cross-section displacements $v(x)$ and $w(x)$:

$$\mathbf{s}(x) = \mathbf{b}(x)\,\mathbf{q} + \mathbf{s}_b(x) \tag{11}$$

being $\mathbf{b}(x)$ the equilibrium matrix, resulting as:

$$\mathbf{b}(x) = \begin{bmatrix} 1 & 0 & 0 & 0 & 0 & 0 \\ v(x) & \frac{x}{L} - 1 & \frac{x}{L} & 0 & 0 & 0 \\ -v'(x) & -\frac{1}{L} & -\frac{1}{L} & 0 & 0 & 0 \\ 0 & 0 & 0 & 1 & 0 & 0 \\ -w(x) & 0 & 0 & 0 & \frac{x}{L} - 1 & \frac{x}{L} \\ -w'(x) & 0 & 0 & 0 & \frac{1}{L} & \frac{1}{L} \end{bmatrix} \tag{12}$$

and where, based on the second-order geometry assumption, the nonlinear coupling between the axial and shear internal forces is neglected in the definition of matrix $\mathbf{b}(x)$. L is the undeformed element length and $\mathbf{s}_b(x)$ are the cross-section stresses due to distributed loads, that is the axial load $b_u(x)$, the transverse loads $b_v(x)$ and $b_w(x)$ in the directions y and z, respectively, and the distributed torque $m_x(x)$. The expressions for $\mathbf{s}_b(x)$ can be derived as particular solution of the equilibrium conditions under distributed loads and zero basic nodal forces $\mathbf{q}$. When these conditions are expressed in the element deformed configuration, with the axial-shear coupling similarly neglected, only the contributions arising from $b_u(x)$ exhibits nonlinearity. Consequently, in this study, all expressions for $\mathbf{s}_b(x)$ are approximated to be equivalent to the analogous linear equilibrium solution obtained under linear geometry [4]. The responsibility for error correction is then delegated to the corotational approach and mesh refinement.

It is worth to mention that more general equilibrated stress interpolations than that in Eqs. (11) and Eq. (12) are also possible, even removing the hypothesis of small rotations. To this end, a particularly convenient approach is that based on the interpolation of spatial stress measures, as suggested in [39,53], as these are always constant along the beam axis, even under nonlinear geometry, as opposed to the local quantities. However, the enhancement of the beam FE formulation is beyond the scope of this work and is not discussed in this paper.

The relationship between the generalized cross-section strains $\mathbf{e}(x)$ and the element basic displacements $\mathbf{v}$ is obtained from the Hellinger–Reissner variational principle [6,44,54] and, given the particular selection of the local corotational reference system (Fig. 1), it results as:

$$\mathbf{v} = \int_0^L \mathbf{b}^{*T}(x)\,\mathbf{e}(x)\,dx \tag{13}$$

where matrix $\mathbf{b}^*(x)$ governs the incremental form of Eq. (11), i.e., $\delta\mathbf{s}(x) = \mathbf{b}^*(x)\,\delta\mathbf{q}$ [47], resulting as:

$$\mathbf{b}^*(x) = \begin{bmatrix} 1 & 0 & 0 & 0 & 0 & 0 \\ \frac{v(x)}{2} & \frac{x}{L} - 1 & \frac{x}{L} & 0 & 0 & 0 \\ -\frac{v'(x)}{2} & -\frac{1}{L} & -\frac{1}{L} & 0 & 0 & 0 \\ 0 & 0 & 0 & 1 & 0 & 0 \\ -\frac{w(x)}{2} & 0 & 0 & 0 & \frac{x}{L} - 1 & \frac{x}{L} \\ -\frac{w'(x)}{2} & 0 & 0 & 0 & \frac{1}{L} & \frac{1}{L} \end{bmatrix} \tag{14}$$

Hence, the element flexibility matrix $\mathbf{f}$ is obtained by differentiating of the element basic displacements with respect to the basic nodal forces and results as [44,47]:

$$\mathbf{f} = \frac{d\mathbf{v}}{d\mathbf{q}} = \int_0^L \left\{\mathbf{b}^{*T}(x)\,\mathbf{f}_s(x)\,[\mathbf{b}(x) + \mathbf{r}(x)] + \mathbf{g}(x)\right\}\,dx \tag{15}$$

being $\mathbf{f}_s(x) = \mathbf{k}_s^{-1}(x)$ the generalized cross-section flexibility matrix, while $\mathbf{r}(x)$ and $\mathbf{g}(x)$ are matrices obtained from the derivatives of $\mathbf{b}(x)$ and $\mathbf{b}^*(x)$ with respect to $\mathbf{q}$ [44,47].

As observed in [6,47], the element flexibility matrix is non-symmetric. However, when computed through quadrature rules in conjunction with the CSBDI, **f** numerically tends to be symmetric, with the anti-symmetric part containing terms that are more than five order of magnitude smaller than those appearing in the symmetric part. This also applies to the FDDI, where the terms of the anti-symmetric part are, in some cases, even smaller, as observed by direct inspection of the values obtained for the applications conducted in this work.

3. Numerical techniques for transverse displacement computation

The integrals in Eqs. (13) and (15) are numerically solved by means of one-dimensional (1D) quadrature schemes (see also Appendix A), which are particularly advantageous, especially for nonlinear constitutive conditions. It results:

$$\mathbf{v} = \sum_{h=1}^{n} \mathbf{b}^{*T}(\xi_h)\,\mathbf{e}(\xi_h)\,w_h \qquad \text{and} \qquad \mathbf{f} = \sum_{h=1}^{n} \left\{ \mathbf{b}^{*T}(\xi_h)\,\mathbf{f}_s(\xi_h)\left[\mathbf{b}(\xi_h) + \mathbf{r}(\xi_h)\right] + \mathbf{g}(\xi_h) \right\} w_h \qquad (16)$$

where $\xi_h = x_h/L$ and w_h (with $h = 1, \dots, n$) are the normalized abscissas and weights of the n quadrature points (cross-sections). Hence, the values of transverse displacements $v(x)$ and $w(x)$ at the quadrature cross-sections, and their derivatives with respect to x and $\mathbf{q}$, are required to compute $\mathbf{v}$ and $\mathbf{f}$.

The CSBDI technique in [44] and the proposed FDDI technique accomplish this task. In the following, these are described referring to the same formal notation, where the transverse displacements and the derivatives with respect to x of all element quadrature cross-sections are collected in the vectors:

$$\mathbf{V} = \left\{ v(\xi_1) \quad v(\xi_2) \quad \dots \quad v(\xi_n) \right\}^T \qquad \text{and} \qquad \mathbf{W} = \left\{ w(\xi_1) \quad w(\xi_2) \quad \dots \quad w(\xi_n) \right\}^T \qquad (17)$$

$$\mathbf{V}' = \left\{ v'(\xi_1) \quad v'(\xi_2) \quad \dots \quad v'(\xi_n) \right\}^T \qquad \text{and} \qquad \mathbf{W}' = \left\{ w'(\xi_1) \quad w'(\xi_2) \quad \dots \quad w'(\xi_n) \right\}^T \qquad (18)$$

The curvatures and shear strains are assumed to be known at the quadrature abscissas and listed in the vectors:

$$\mathbf{X}_z = \left\{ \chi_z(\xi_1) \quad \chi_z(\xi_2) \quad \dots \quad \chi_z(\xi_n) \right\}^T \qquad \text{and} \qquad \boldsymbol{\Gamma}_y = \left\{ \gamma_y(\xi_1) \quad \gamma_y(\xi_2) \quad \dots \quad \gamma_y(\xi_n) \right\}^T \qquad (19)$$

$$\mathbf{X}_y = \left\{ \chi_y(\xi_1) \quad \chi_y(\xi_2) \quad \dots \quad \chi_y(\xi_n) \right\}^T \qquad \text{and} \qquad \boldsymbol{\Gamma}_z = \left\{ \gamma_z(\xi_1) \quad \gamma_z(\xi_2) \quad \dots \quad \gamma_z(\xi_n) \right\}^T \qquad (20)$$

Hence, according to both techniques, $\mathbf{V}$, $\mathbf{W}$, $\mathbf{V}'$, $\mathbf{W}'$ can be expressed in terms of $\mathbf{X}_z$, $\boldsymbol{\Gamma}_y$, $\mathbf{X}_y$ and $\boldsymbol{\Gamma}_z$ as:

$$\mathbf{V} = \mathbf{H}_\chi \mathbf{X}_z + \mathbf{H}_\gamma \boldsymbol{\Gamma}_y \qquad \text{and} \qquad \mathbf{W} = -\mathbf{H}_\chi \mathbf{X}_y + \mathbf{H}_\gamma \boldsymbol{\Gamma}_z \qquad (21)$$

$$\mathbf{V}' = \mathbf{H}'_\chi \mathbf{X}_z + \mathbf{H}'_\gamma \boldsymbol{\Gamma}_y \qquad \text{and} \qquad \mathbf{W}' = -\mathbf{H}'_\chi \mathbf{X}_y + \mathbf{H}'_\gamma \boldsymbol{\Gamma}_z \qquad (22)$$

where matrices $\mathbf{H}_\chi$, $\mathbf{H}'_\chi$, $\mathbf{H}_\gamma$ and $\mathbf{H}'_\gamma$ are defined differently depending on whether one or the other technique is applied, as discussed in the two following subsections.

Finally, the derivatives with respect to $\mathbf{q}$ of all quadrature cross-sections result in the matrices $\mathbf{V}_{,\mathbf{q}} = \frac{d\mathbf{V}}{d\mathbf{q}}$, $\mathbf{V}'_{,\mathbf{q}} = \frac{d\mathbf{V}'}{d\mathbf{q}}$, $\mathbf{W}_{,\mathbf{q}} = \frac{d\mathbf{W}}{d\mathbf{q}}$ and $\mathbf{W}'_{,\mathbf{q}} = \frac{d\mathbf{W}'}{d\mathbf{q}}$. These are computed following the same procedure as in [44,47]. In particular, if the compact form $\mathbf{Y}_{,\mathbf{q}} = \left[\mathbf{V}_{,\mathbf{q}}^T \quad \mathbf{V}'^T_{,\mathbf{q}} \quad \mathbf{W}_{,\mathbf{q}}^T \quad \mathbf{W}'^T_{,\mathbf{q}} \right]^T$ is introduced, it results:

$$\mathbf{Y}_{,\mathbf{q}} = \left(\mathbf{I}_{4n} - p_{xj}\,\bar{\mathbf{H}}\,\bar{\bar{\mathbf{F}}}_s \right)^{-1} \left(\bar{\mathbf{H}}\,\bar{\mathbf{F}}_s\,\bar{\mathbf{B}} \right) \qquad (23)$$

where $\mathbf{I}_{4n}$ is a 4×4 identity matrix, while:

$$\bar{\mathbf{H}} = \begin{bmatrix} \mathbf{H}_\chi & \mathbf{H}_\gamma & \mathbf{O}_n & \mathbf{O}_n \\ \mathbf{H}'_\chi & \mathbf{H}'_\gamma & \mathbf{O}_n & \mathbf{O}_n \\ \mathbf{O}_n & \mathbf{O}_n & -\mathbf{H}_\chi & \mathbf{H}_\gamma \\ \mathbf{O}_n & \mathbf{O}_n & -\mathbf{H}'_\chi & \mathbf{H}'_\gamma \end{bmatrix} \qquad \text{and} \qquad \bar{\mathbf{B}} = \begin{bmatrix} \mathbf{b}(\xi_1) \\ \mathbf{b}(\xi_2) \\ \vdots \\ \mathbf{b}(\xi_n) \end{bmatrix} \qquad (24)$$

Matrices $\bar{\mathbf{F}}_s$ and $\bar{\bar{\mathbf{F}}}_s$ collect the quadrature cross-section flexibility matrices according to the definitions in [47]. Further details can be found in this reference paper.

3.1. Review of the CSBDI technique

In the CSBDI, the curvatures and shear strains are interpolated along the element axis through Lagrange polynomials (Fig. 2). These polynomials are collected in the row vector $\boldsymbol{\Lambda}(\xi) = \left[\lambda_1(\xi) \quad \lambda_2(\xi) \quad \dots \quad \lambda_n(\xi) \right]$, which gives rise to the following expressions:

$$\chi_z(\xi) = \boldsymbol{\Lambda}(\xi)\,\mathbf{X}_z \qquad \text{and} \qquad \gamma_y(\xi) = \boldsymbol{\Lambda}(\xi)\,\boldsymbol{\Gamma}_y \qquad (25)$$

$$\chi_y(\xi) = \boldsymbol{\Lambda}(\xi)\,\mathbf{X}_y \qquad \text{and} \qquad \gamma_z(\xi) = \boldsymbol{\Lambda}(\xi)\,\boldsymbol{\Gamma}_z \qquad (26)$$

The cross-section compatibility conditions in Eq. (6) impose that:

$$v''(x) = \chi_z(x) + \gamma'_y(x) \qquad \text{and} \qquad w''(x) = -\chi_y(x) + \gamma'_z(x) \qquad (27)$$
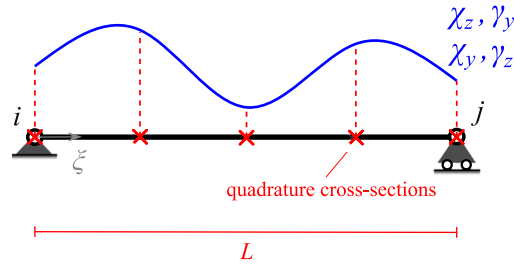
Fig. 2. Schematic of the curvatures and shear strains interpolation along the element axis.

After expressing in ξ, the integration of these equations, with the introduction of the boundary conditions and Eqs. (25) and (26), gives [44,47]:

$$v(\xi) = \mathbf{h}_\chi(\xi)\mathbf{X}_z + \mathbf{h}_\gamma(\xi)\boldsymbol{\Gamma}_y \qquad \text{and} \qquad w(\xi) = -\mathbf{h}_\chi(\xi)\mathbf{X}_y + \mathbf{h}_\gamma(\xi)\boldsymbol{\Gamma}_z \tag{28}$$

where $\mathbf{h}_\chi(\xi)$ and $\mathbf{h}_\gamma(\xi)$ are row vectors that collects the integrals of the Lagrange polynomials [44,47]. These are defined by introducing the Vandermonde matrix $\mathbf{G}$ of the quadrature cross-section abscissas [34,44], i.e.:

$$\mathbf{G} = \begin{bmatrix} 1 & \xi_1 & \xi_1^2 & \cdots & \xi_1^{n-1} \\ 1 & \xi_2 & \xi_2^2 & \cdots & \xi_2^{n-1} \\ \vdots & \vdots & \vdots & \ddots & \vdots \\ 1 & \xi_n & \xi_n^2 & \cdots & \xi_n^{n-1} \end{bmatrix} \tag{29}$$

which leads to the following expressions:

$$\mathbf{h}_\chi(\xi) = L^2 \left[\frac{1}{2}\left(\xi^2 - \xi\right) \quad \frac{1}{6}\left(\xi^3 - \xi\right) \quad \cdots \quad \frac{1}{n(n+1)}\left(\xi^{n+1} - \xi\right) \right] \mathbf{G}^{-1} \tag{30}$$

$$\mathbf{h}_\gamma(\xi) = L \left[0 \quad \frac{1}{2}\left(\xi^2 - \xi\right) \quad \cdots \quad \frac{1}{n}\left(\xi^n - \xi\right) \right] \mathbf{G}^{-1} \tag{31}$$

$$\mathbf{h}'_\chi(\xi) = L^2 \left[\left(\xi - \frac{1}{2}\right) \quad \frac{1}{2}\left(\xi^2 - \frac{1}{3}\right) \quad \cdots \quad \frac{1}{n}\left(\xi^n - \frac{1}{n+1}\right) \right] \mathbf{G}^{-1} \tag{32}$$

$$\mathbf{h}'_\gamma(\xi) = L \left[0 \quad \left(\xi - \frac{1}{2}\right) \quad \cdots \quad \left(\xi^{n-1} - \frac{1}{n}\right) \right] \mathbf{G}^{-1} \tag{33}$$

Thus, by evaluating Eq. (28) for all quadrature cross-sections, the expressions in Eqs. (21) and (22) are obtained, where the matrices $\mathbf{H}_\chi$, $\mathbf{H}'_\chi$, $\mathbf{H}_\gamma$ and $\mathbf{H}'_\gamma$ result as:

$$\mathbf{H}_\chi = \begin{bmatrix} \mathbf{h}_\chi(\xi_1) \\ \mathbf{h}_\chi(\xi_2) \\ \vdots \\ \mathbf{h}_\chi(\xi_n) \end{bmatrix}, \quad \mathbf{H}_\gamma = \begin{bmatrix} \mathbf{h}_\gamma(\xi_1) \\ \mathbf{h}_\gamma(\xi_2) \\ \vdots \\ \mathbf{h}_\gamma(\xi_n) \end{bmatrix}, \quad \mathbf{H}'_\chi = \begin{bmatrix} \mathbf{h}'_\chi(\xi_1) \\ \mathbf{h}'_\chi(\xi_2) \\ \vdots \\ \mathbf{h}'_\chi(\xi_n) \end{bmatrix} \quad \text{and} \quad \mathbf{H}'_\gamma = \begin{bmatrix} \mathbf{h}'_\gamma(\xi_1) \\ \mathbf{h}'_\gamma(\xi_2) \\ \vdots \\ \mathbf{h}'_\gamma(\xi_n) \end{bmatrix} \tag{34}$$

i.e., these contain the evaluation of the matrices $\mathbf{h}_\chi(\xi)$, $\mathbf{h}'_\chi(\xi)$, $\mathbf{h}_\gamma(\xi)$ and $\mathbf{h}'_\gamma(\xi)$ at all quadrature abscissas.

As pointed out in [37], the CSBDI technique may encounter numerical issues when a large number of quadrature cross-sections are used along the element. This is because, in this case, an oscillatory Lagrange interpolation of the curvatures and shear strains can induce oscillatory variation of the displacements and lead to incorrect solutions. Scott and Denavit [46] showed that this problem is irrelevant if a small number of quadrature cross-sections are used, focusing their study on the common case where $n = 5$.

The numerical analyses conducted in this work and presented in Section 5 examine the accuracy of the CSBDI in this regard. However, an important aspect deserves to be discussed. As indicated in Eqs. (30) to (33), the computation of the matrices $\mathbf{H}_\chi$, $\mathbf{H}'_\chi$, $\mathbf{H}_\gamma$ and $\mathbf{H}'_\gamma$ requires the inverse of the matrix $\mathbf{G}$. When the integration rule uses many quadrature cross-sections, matrix $\mathbf{G}$ becomes badly conditioned, i.e., it results nearly singular and numerically difficult to invert. Fig. 3 shows the variation of the reciprocal condition number $r_c(\mathbf{G})$ of this matrix when the number of quadrature cross-sections n increases from 2 to 14. $r_c(\mathbf{G})$ is a scalar close to 0 when $\mathbf{G}$ is nearly singular and badly conditioned, and close to 1 when $\mathbf{G}$ is well conditioned [55]. The plotted values are computed in Matlab (*rcond* function) for three different distributions of the quadrature cross-sections along L, i.e., an equally spaced distribution (solid blue curve) that includes the end points (as in the Trapezoidal or Simpson quadrature scheme), and the two distributions corresponding to the Gauss–Legendre (dashed black curve) and Gauss–Lobatto (dashed red curve) quadrature schemes. The figure shows that, when $n > 7$, the reciprocal condition number is very close to 0 (for $n = 7$, it results $r_c(\mathbf{G}) = 0.00001159$ for the equally spaced distribution, $r_c(\mathbf{G}) = 0.00322148$ for the Gauss–Legendre distribution, and $r_c(\mathbf{G}) = 0.00463530$ for the Gauss–Lobatto distribution) and tends to vanish when the number of cross-sections is increased, that is, $\mathbf{G}$ tends to be singular.

3.2. Proposed FDDI technique

The proposed Finite Difference Displacement Integration (FDDI) technique is based on the idea that the cross-section compatibility conditions in Eq. (27), when imposed at the quadrature cross-sections, can be expressed through FD approximations of the
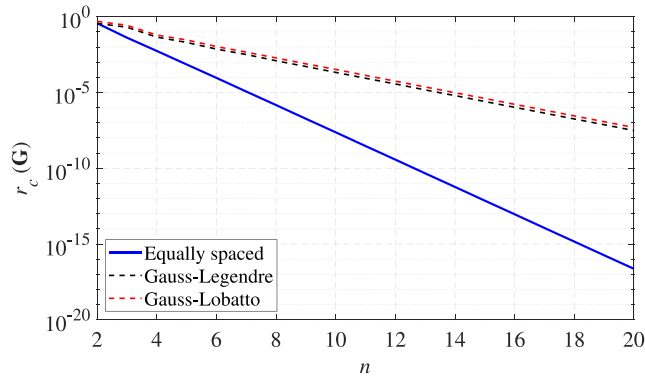
Fig. 3. Variation of the reciprocal condition number of the Vandermonde matrix **G** with respect to the number n of quadrature cross-sections.

transverse displacement second order derivatives, i.e., by means of proper linear combinations of the transverse displacements in **V** and **W** [54,56–58]. For the hth quadrature cross-section, these approximations are written as:

$$v''(\xi_h) \approx \sum_{j=1}^{n} \delta_{hj}^2 \, v(\xi_j) = \left\{ \delta_{h1}^2 \quad \delta_{h2}^2 \quad \ldots \quad \delta_{hn}^2 \right\} \mathbf{V} \tag{35}$$

$$w''(\xi_h) \approx \sum_{j=1}^{n} \delta_{hj}^2 \, w(\xi_j) = \left\{ \delta_{h1}^2 \quad \delta_{h2}^2 \quad \ldots \quad \delta_{hn}^2 \right\} \mathbf{W} \tag{36}$$

where $\delta_{h1}^2, \delta_{h2}^2, \ldots, \delta_{hn}^2$ are the FD coefficients that define the second order derivative approximation. It has to be noted that the superscript of the symbols δ here indicate the derivative order to be approximated. Hence, it results:

$$\left\{ \delta_{h1}^2 \quad \delta_{h2}^2 \quad \ldots \quad \delta_{hn}^2 \right\} \mathbf{V} = \chi_z(\xi_h) + \gamma'_y(\xi_h) \tag{37}$$

$$\left\{ \delta_{h1}^2 \quad \delta_{h2}^2 \quad \ldots \quad \delta_{hn}^2 \right\} \mathbf{W} = -\chi_y(\xi_h) + \gamma'_z(\xi_h) \tag{38}$$

The first order derivatives of the shear strains, $\gamma'_y(\xi_h)$ and $\gamma'_z(\xi_h)$, are similarly approximated by exploiting the FD approach, i.e.:

$$\gamma'_y(\xi_h) \approx \sum_{j=1}^{n} \delta_{hj}^1 \, \gamma_y(\xi_j) = \left\{ \delta_{h1}^1 \quad \delta_{h2}^1 \quad \ldots \quad \delta_{hn}^1 \right\} \boldsymbol{\Gamma}_y \tag{39}$$

$$\gamma'_z(\xi_h) \approx \sum_{j=1}^{n} \delta_{hj}^1 \, \gamma_z(\xi_j) = \left\{ \delta_{h1}^1 \quad \delta_{h2}^1 \quad \ldots \quad \delta_{hn}^1 \right\} \boldsymbol{\Gamma}_z \tag{40}$$

where $\delta_{h1}^1, \delta_{h2}^1, \ldots, \delta_{hn}^1$ are the FD coefficients that define the first order derivative approximation. Hence, it results:

$$\left\{ \delta_{h1}^2 \quad \delta_{h2}^2 \quad \ldots \quad \delta_{hn}^2 \right\} \mathbf{V} = \chi_z(\xi_h) + \left\{ \delta_{h1}^1 \quad \delta_{h2}^1 \quad \ldots \quad \delta_{hn}^1 \right\} \boldsymbol{\Gamma}_y \tag{41}$$

$$\left\{ \delta_{h1}^2 \quad \delta_{h2}^2 \quad \ldots \quad \delta_{hn}^2 \right\} \mathbf{W} = -\chi_y(\xi_h) + \left\{ \delta_{h1}^1 \quad \delta_{h2}^1 \quad \ldots \quad \delta_{hn}^1 \right\} \boldsymbol{\Gamma}_z \tag{42}$$

Eqs. (41) and (42) are written for all quadrature cross-sections in the following matrix forms:

$$\underbrace{\begin{bmatrix} \delta_{11}^2 & \delta_{12}^2 & \cdots & \delta_{1n}^2 \\ \delta_{21}^2 & \delta_{22}^2 & \cdots & \delta_{2n}^2 \\ \vdots & \vdots & \ddots & \vdots \\ \delta_{n1}^2 & \delta_{n2}^2 & \cdots & \delta_{nn}^2 \end{bmatrix}}_{\boldsymbol{\Delta}^2} \underbrace{\begin{Bmatrix} v(\xi_1) \\ v(\xi_2) \\ \vdots \\ v(\xi_n) \end{Bmatrix}}_{\mathbf{V}} = \underbrace{\begin{Bmatrix} \chi_z(\xi_1) \\ \chi_z(\xi_2) \\ \vdots \\ \chi_z(\xi_n) \end{Bmatrix}}_{\mathbf{X}_z} + \underbrace{\begin{bmatrix} \delta_{11}^1 & \delta_{12}^1 & \cdots & \delta_{1n}^1 \\ \delta_{21}^1 & \delta_{22}^1 & \cdots & \delta_{2n}^1 \\ \vdots & \vdots & \ddots & \vdots \\ \delta_{n1}^1 & \delta_{n2}^1 & \cdots & \delta_{nn}^1 \end{bmatrix}}_{\boldsymbol{\Delta}^1} \underbrace{\begin{Bmatrix} \gamma_y(\xi_1) \\ \gamma_y(\xi_2) \\ \vdots \\ \gamma_y(\xi_n) \end{Bmatrix}}_{\boldsymbol{\Gamma}_y} \tag{43}$$

$$\underbrace{\begin{bmatrix} \delta_{11}^2 & \delta_{12}^2 & \cdots & \delta_{1n}^2 \\ \delta_{21}^2 & \delta_{22}^2 & \cdots & \delta_{2n}^2 \\ \vdots & \vdots & \ddots & \vdots \\ \delta_{n1}^2 & \delta_{n2}^2 & \cdots & \delta_{nn}^2 \end{bmatrix}}_{\boldsymbol{\Delta}^2} \underbrace{\begin{Bmatrix} w(\xi_1) \\ w(\xi_2) \\ \vdots \\ w(\xi_n) \end{Bmatrix}}_{\mathbf{W}} = -\underbrace{\begin{Bmatrix} \chi_y(\xi_1) \\ \chi_y(\xi_2) \\ \vdots \\ \chi_y(\xi_n) \end{Bmatrix}}_{\mathbf{X}_y} + \underbrace{\begin{bmatrix} \delta_{11}^1 & \delta_{12}^1 & \cdots & \delta_{1n}^1 \\ \delta_{21}^1 & \delta_{22}^1 & \cdots & \delta_{2n}^1 \\ \vdots & \vdots & \ddots & \vdots \\ \delta_{n1}^1 & \delta_{n2}^1 & \cdots & \delta_{nn}^1 \end{bmatrix}}_{\boldsymbol{\Delta}^1} \underbrace{\begin{Bmatrix} \gamma_z(\xi_1) \\ \gamma_z(\xi_2) \\ \vdots \\ \gamma_z(\xi_n) \end{Bmatrix}}_{\boldsymbol{\Gamma}_z} \tag{44}$$

where matrices $\boldsymbol{\Delta}^2$ and $\boldsymbol{\Delta}^1$ collect all the FD coefficients for the second and first order derivative approximations, respectively, which depend only on the quadrature cross-section abscissas. The method used for their computation is discussed in the following subsection, although the previous expressions are generally valid.
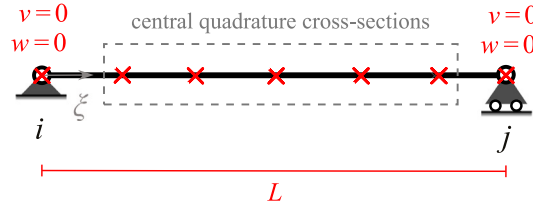
8

Fig. 4. Partition between the central and the end quadrature cross-sections.

As mentioned, the curvatures and shear strains, $\mathbf{X}_z$, $\boldsymbol{\Gamma}_y$, $\mathbf{X}_z$ and $\boldsymbol{\Gamma}_z$, on the right hand side of Eqs. (43) and (44) are supposed to be known. Hence, the quadrature cross-section displacements, $\mathbf{V}$ and $\mathbf{W}$, on the left-hand side, could be computed by inverting matrix $\boldsymbol{\Delta}^2$. However, inversion of the matrix $\boldsymbol{\Delta}^2$ is not always possible, and a proper modification of Eqs. (43) and (44) is required, as described below.

It is assumed that the quadrature scheme used for the FE numerical integration always includes the two points located at the elements ends, e.g., in the Gauss–Lobatto, Trapezoidal or Simpson quadrature rule, and that at least 3 quadrature cross-sections are considered, $n \geq 3$. Although this represents a limitation of the proposed FDDI technique, this circumstance is very common in practical nonlinear beam FE analysis, as the direct monitoring of the element end cross-sections, where stresses usually assume their maximum values, is often required [5,30,59]. For example, the Gauss–Lobatto quadrature rule with $n = 4$ or $n = 5$ is often adopted.

Under this assumption, due to the simply-supported restraint configuration used to define the basic element displacements in the local reference system (Fig. 4), the transverse displacements of the end quadrature cross-sections are zero and do not need to be computed.

Thus, Eqs. (43) and (44) are rewritten by expressing the compatibility conditions of Eqs. (41) and (42) only for the central quadrature cross-sections ($h = 2, \dots, n-1$) and considering that $v(\xi_1) = v(\xi_n) = w(\xi_1) = w(\xi_n) = 0$, i.e., the coefficients associated to $v(\xi_1)$, $v(\xi_n)$, $w(\xi_1)$ and $w(\xi_n)$ are eliminated from $\boldsymbol{\Delta}^2$, (first and last columns of the matrix). Hence, it results:

$$
\underbrace{\begin{bmatrix} \delta^2_{22} & \cdots & \delta^2_{2\,n-1} \\ \vdots & \ddots & \vdots \\ \delta^2_{n-1\,2} & \cdots & \delta^2_{n-1\,n-1} \end{bmatrix}}_{\boldsymbol{\Delta}^2_c} \underbrace{\begin{Bmatrix} v(\xi_2) \\ \vdots \\ v(\xi_{n-1}) \end{Bmatrix}}_{\mathbf{V}_c} = \underbrace{\begin{Bmatrix} \chi_z(\xi_2) \\ \vdots \\ \chi_z(\xi_{n-1}) \end{Bmatrix}}_{\mathbf{X}_{zc}} + \underbrace{\begin{bmatrix} \delta^1_{21} & \delta^1_{22} & \cdots & \delta^1_{2n} \\ \vdots & \vdots & \ddots & \vdots \\ \delta^1_{n-1\,1} & \delta^1_{n-1\,2} & \cdots & \delta^1_{n-1\,n} \end{bmatrix}}_{\boldsymbol{\Delta}^1_c} \underbrace{\begin{Bmatrix} \gamma_y(\xi_1) \\ \gamma_y(\xi_2) \\ \vdots \\ \gamma_y(\xi_n) \end{Bmatrix}}_{\boldsymbol{\Gamma}_y} \tag{45}
$$

$$
\underbrace{\begin{bmatrix} \delta^2_{22} & \cdots & \delta^2_{2\,n-1} \\ \vdots & \ddots & \vdots \\ \delta^2_{n-1\,2} & \cdots & \delta^2_{n-1\,n-1} \end{bmatrix}}_{\boldsymbol{\Delta}^2_c} \underbrace{\begin{Bmatrix} w(\xi_2) \\ \vdots \\ w(\xi_{n-1}) \end{Bmatrix}}_{\mathbf{W}_c} = -\underbrace{\begin{Bmatrix} \chi_y(\xi_2) \\ \vdots \\ \chi_y(\xi_{n-1}) \end{Bmatrix}}_{\mathbf{X}_{yc}} + \underbrace{\begin{bmatrix} \delta^1_{21} & \delta^1_{22} & \cdots & \delta^1_{2n} \\ \vdots & \vdots & \ddots & \vdots \\ \delta^1_{n-1\,1} & \delta^1_{n-1\,2} & \cdots & \delta^1_{n-1\,n} \end{bmatrix}}_{\boldsymbol{\Delta}^1_c} \underbrace{\begin{Bmatrix} \gamma_z(\xi_1) \\ \gamma_z(\xi_2) \\ \vdots \\ \gamma_z(\xi_n) \end{Bmatrix}}_{\boldsymbol{\Gamma}_z} \tag{46}
$$

In other words, vectors $\mathbf{V}$, $\mathbf{W}$, $\mathbf{X}_z$ and $\mathbf{X}_y$ are partitioned as follows, by separating the end from the central cross-section values:

$$
\mathbf{V} = \left\{ v(\xi_1) \quad \mathbf{V}_c^T \quad v(\xi_n) \right\}^T = \left\{ 0 \quad \mathbf{V}_c^T \quad 0 \right\}^T \quad \text{and} \quad \mathbf{W} = \left\{ w(\xi_1) \quad \mathbf{W}_c^T \quad w(\xi_n) \right\}^T = \left\{ 0 \quad \mathbf{W}_c^T \quad 0 \right\}^T \tag{47}
$$

$$
\mathbf{X}_z = \left\{ \chi_z(\xi_1) \quad \mathbf{X}_{zc}^T \quad \chi_z(\xi_n) \right\}^T \quad \text{and} \quad \mathbf{X}_y = \left\{ \chi_y(\xi_1) \quad \mathbf{X}_{yc}^T \quad \chi_y(\xi_n) \right\}^T \tag{48}
$$

and, only $\mathbf{V}_c$ and $\mathbf{W}_c$ are determined from the compatibility conditions written only for the central quadrature cross-sections, i.e.:

$$
\mathbf{V}_c = \left(\boldsymbol{\Delta}^2_c \right)^{-1} \mathbf{X}_{zc} + \left(\boldsymbol{\Delta}^2_c \right)^{-1} \boldsymbol{\Delta}^1_c \boldsymbol{\Gamma}_y \quad \text{and} \quad \mathbf{W}_c = -\left(\boldsymbol{\Delta}^2_c \right)^{-1} \mathbf{X}_{yc} + \left(\boldsymbol{\Delta}^2_c \right)^{-1} \boldsymbol{\Delta}^1_c \boldsymbol{\Gamma}_z \tag{49}
$$

This approach is the classic second order derivative FD approximation of a function defined over a 1D domain with the introduction of homogeneous Dirichlet boundary conditions, i.e, when the function assumes zero values at the ends of the domain. Thus, it can be proved that matrix $\boldsymbol{\Delta}^2_c$ is always non-singular [58].

Hence, by re-introducing the zero end values, the matrices $\mathbf{H}_\chi$ and $\mathbf{H}_\gamma$ relating $\mathbf{V}$ and $\mathbf{W}$ to $\mathbf{X}_z$, $\boldsymbol{\Gamma}_y$, $\mathbf{X}_y$ and $\boldsymbol{\Gamma}_z$, as required in Eq. (21), result as:

$$
\mathbf{H}_\chi = \begin{bmatrix} & \mathbf{O}_n & \\ \mathbf{O}_{n-2} & \left(\boldsymbol{\Delta}^2_c \right)^{-1} & \mathbf{O}_{n-2} \\ & \mathbf{O}_n & \end{bmatrix} \quad \text{and} \quad \mathbf{H}_\gamma = \begin{bmatrix} \mathbf{O}_n \\ \left(\boldsymbol{\Delta}^2_c \right)^{-1} \boldsymbol{\Delta}^1_c \\ \mathbf{O}_n \end{bmatrix} \tag{50}
$$

being $\mathbf{O}_n$ a zero row vector with length n, and $\mathbf{O}_{n-2}$ a zero column vector with length $n - 2$.
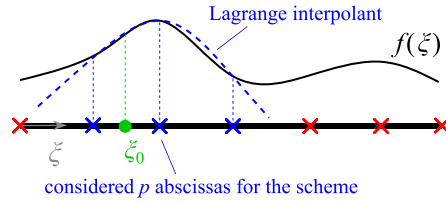
Fig. 5. Example of Lagrange interpolation approach (3-point scheme) for FD coefficients.

To define the matrices $\mathbf{H}'_\chi$ and $\mathbf{H}'_\gamma$ that relate $\mathbf{V}'$ and $\mathbf{W}'$ to $\mathbf{X}_z$, $\boldsymbol{\Gamma}_y$, $\mathbf{X}_y$ and $\boldsymbol{\Gamma}_z$ in Eq. (22), the FD first order derivative approximation is exploited, similarly to Eqs. (39) and (40), i.e., for the hth quadrature cross-section, it results:

$$v'(\xi_h) \approx \sum_{j=1}^{n} \delta_{hj}^1 v(\xi_j) = \left\{ \delta_{h1}^1 \quad \delta_{h2}^1 \quad \ldots \quad \delta_{hn}^1 \right\} \mathbf{V} \tag{51}$$

$$w'(\xi_h) \approx \sum_{j=1}^{n} \delta_{hj}^1 w(\xi_j) = \left\{ \delta_{h1}^1 \quad \delta_{h2}^1 \quad \ldots \quad \delta_{hn}^1 \right\} \mathbf{W} \tag{52}$$

which are written for all quadrature cross-section in compact matrix form as:

$$\mathbf{V}' = \boldsymbol{\Delta}^1 \mathbf{V} = \boldsymbol{\Delta}^1 \left(\mathbf{H}_\chi \mathbf{X}_z + \mathbf{H}_\gamma \boldsymbol{\Gamma}_y \right) \qquad \text{and} \qquad \mathbf{W}' = \boldsymbol{\Delta}^1 \mathbf{W} = \boldsymbol{\Delta}^1 \left(-\mathbf{H}_\chi \mathbf{X}_y + \mathbf{H}_\gamma \boldsymbol{\Gamma}_z \right) \tag{53}$$

where Eq. (21) is used to express $\mathbf{V}$ and $\mathbf{W}$. Hence, it finally results:

$$\mathbf{H}'_\chi = \boldsymbol{\Delta}^1 \mathbf{H}_\chi \qquad \text{and} \qquad \mathbf{H}'_\gamma = \boldsymbol{\Delta}^1 \mathbf{H}_\gamma \tag{54}$$

3.3. Computation of the FD coefficients for different schemes

In general, given a 1D function $f(\xi)$ and the values that this assumes at n abscissas $\xi_1, \xi_2, \ldots, \xi_n$, two approaches can be used to compute the FD coefficients, $\delta_{01}^m, \delta_{02}^m, \ldots, \delta_{0n}^m$, that approximate the derivative of order m of $f(\xi)$, evaluated at the general abscissa ξ_0 (not necessarily coinciding with one of the n abscissas where $f(\xi)$ is known), i.e.:

$$\left. \frac{\mathrm{d}^m f(\xi)}{\mathrm{d} \xi^m} \right|_{\xi=\xi_0} \approx \sum_{q=1}^{n} \delta_{0q}^m f(\xi_q) = \left\{ \delta_{01}^m \quad \delta_{02}^m \quad \ldots \quad \delta_{0n}^m \right\} \begin{Bmatrix} f(\xi_1) \\ f(\xi_2) \\ \vdots \\ f(\xi_n) \end{Bmatrix} \tag{55}$$

The first approach is that of the *Undetermined coefficients*, which is based on the Taylor expansion of the derivative to be approximated at the point. The second is the *Lagrange interpolation* approach [58]. This latter is considered in this work as it is more general and better suitable for code implementation. The approach starts with the choice of p of the n abscissas where $f(\xi)$ is known. These define the FD *scheme* for the derivative approximation (p-point FD scheme). An example is shown in Fig. 5, where a 3-point scheme is considered and the selected $p = 3$ abscissas are highlighted in blue. Hence, the function $f(\xi)$ is approximated by constructing its Lagrange interpolation over the p abscissas, i.e.:

$$f(\xi) \approx \sum_{q=1}^{p} \lambda_q(\xi) f(\xi_q) \tag{56}$$

where $\lambda_1(\xi), \lambda_2(\xi), \ldots, \lambda_p(\xi)$ are the Lagrange polynomials associated to the p abscissas.

Eq. (56) can be written in a similar but extended form that involves all the n abscissas, that is:

$$f(\xi) \approx \sum_{q=1}^{n} \lambda_q(\xi) f(\xi_q) = \left\{ \lambda_1(\xi) \quad \lambda_2(\xi) \quad \ldots \quad \lambda_n(\xi) \right\} \begin{Bmatrix} f(\xi_1) \\ f(\xi_2) \\ \vdots \\ f(\xi_n) \end{Bmatrix} \tag{57}$$

where the interpolation polynomials associated to the $n - p$ abscissas not belonging to the FD scheme are assumed as null uniform functions.

Hence, the FD coefficient δ_{0q}^m associated to the qth abscissa is computed as the m order derivative of the corresponding Lagrange polynomial $\lambda_q(\xi)$ evaluated in ξ_0, i.e.:

$$\delta_{0q}^m = \left. \frac{\mathrm{d}^m \lambda_q(\xi)}{\mathrm{d} \xi^m} \right|_{\xi=\xi_0} \qquad \text{for} \quad q = 1, \ldots, n \tag{58}$$

In general, this is non-zero only for the p abscissas belonging to the scheme (except special cases where the derivative in Eq. (58) however gives null coefficient $\delta^m_{0\,q}$; see, for instance, Eq. (62)).

When the derivatives are defined with respect to x, with $x = \xi L$, as it occurs in the expressions introduced in Section 3.2, this definition is modified by recalling that:

$$\frac{\mathrm{d}^m \lambda_q(\xi)}{\mathrm{d} x^m} = \frac{\mathrm{d}^m \lambda_q(\xi)}{\mathrm{d} \xi^m} \left(\frac{\mathrm{d}^m \xi}{\mathrm{d} x^m} \right)^m = \frac{\mathrm{d}^m \lambda_q(\xi)}{\mathrm{d} \xi^m} \frac{1}{L^m} \tag{59}$$

Accordingly, the FD coefficients introduced in Section 3.2 to approximate the second- and first-order derivatives result from the derivatives of the Lagrange polynomials constructed over the quadrature cross-section abscissas. In other words, to approximate the derivatives at the hth quadrature cross-section (i.e., to compute the hth row of matrices $\boldsymbol{\Delta}^2$ and $\boldsymbol{\Delta}^1$), it is set $\xi_0 = \xi_h$, and thus:

$$\left\{ \delta^2_{h\,1} \quad \delta^2_{h\,2} \quad \cdots \quad \delta^2_{h\,n} \right\} = \left\{ \left. \frac{1}{L^2} \frac{\mathrm{d}^2 \lambda_1(\xi)}{\mathrm{d} \xi^2} \right|_{\xi=\xi_h} \quad \left. \frac{1}{L^2} \frac{\mathrm{d}^2 \lambda_2(\xi)}{\mathrm{d} \xi^2} \right|_{\xi=\xi_h} \quad \cdots \quad \left. \frac{1}{L^2} \frac{\mathrm{d}^2 \lambda_n(\xi)}{\mathrm{d} \xi^2} \right|_{\xi=\xi_h} \right\} \tag{60}$$

$$\left\{ \delta^1_{h\,1} \quad \delta^1_{h\,2} \quad \cdots \quad \delta^1_{h\,n} \right\} = \left\{ \left. \frac{1}{L} \frac{\mathrm{d} \lambda_1(\xi)}{\mathrm{d} \xi} \right|_{\xi=\xi_h} \quad \left. \frac{1}{L} \frac{\mathrm{d} \lambda_2(\xi)}{\mathrm{d} \xi} \right|_{\xi=\xi_h} \quad \cdots \quad \left. \frac{1}{L} \frac{\mathrm{d} \lambda_n(\xi)}{\mathrm{d} \xi} \right|_{\xi=\xi_h} \right\} \tag{61}$$

The computation of these coefficients is straightforward when the quadrature cross-sections are equally spaced along the element axis and some examples are given in the following subsection. However, this is not easy for non-uniformly distributed cross-sections, as it usually results for the most commonly used quadrature rules. In these situations, the computation is carried out efficiently through the recursive algorithm developed by Fornberg [60], which is described in detail in Appendix B. The *Supplementary material* of this paper includes the Matlab function `Fornberg.m`, which performs this computation (see also Appendix C).

Note that, regardless of the total number n of quadrature cross-sections, the higher is p, i.e., the higher is the FD scheme, the higher is the accuracy of the solution [60]. Specific analyses are conducted in Section 4 to investigate this aspect. Moreover, for all numerical tests in Section 5, the solution is always calculated for different FD schemes to study the influence of their accuracy.

The following subsection illustrates three fundamental cases that cover most of the possible practical situations for both linear elastic and nonlinear analyses. However, in general, any scheme is possible.

3.4. Fundamental FDDI schemes

Three fundamental schemes are described in the following, i.e. the 3-point ($p = 3$), 4-point ($p = 4$) and 5-point ($p = 5$) scheme. These can be used for any number n of quadrature cross-sections, given that $p \leq n$. Matlab files associated to this paper as *Supplementary material* (Appendix C) can be used to compute the matrices $\mathbf{H}_\chi$, $\mathbf{H}'_\chi$, $\mathbf{H}_\gamma$ and $\mathbf{H}'_\gamma$ (Eqs. (21) and (22)) with these schemes.

3.4.1. The 3-point scheme (FDDI3)

The 3-point scheme (hereafter indicated as FDDI3) constructs the FD approximation at the hth quadrature cross-section, that is, at ξ_h, over 3 consecutive abscissas that always include ξ_h.

Referring to Fig. 6, when the considered h^{th} quadrature cross-section is a central one (e.g., Fig. 6(b) depicted for the case $h = 3$) the scheme defines the order-2 Lagrange interpolant over the 3 consecutive abscissas $[\xi_{h-1}, \xi_h, \xi_{h+1}]$ (centered scheme). Hence, only the FD coefficients associated to them (blue crosses in the figure) have non-zero values, as opposed to those associated to the remaining $n - 3$ abscissas (red crosses in the figure). By contrast, when the considered h^{th} quadrature cross-section is at the ends (Fig. 6(a) and Fig. 6(b)) the scheme defines the order-2 Lagrange interpolant over the 3 consecutive abscissas $[\xi_h, \xi_{h+1}, \xi_{h+2}]$ (forward scheme), for $\xi_h = 0$, i.e. at i, and $[\xi_{h-2}, \xi_{h-1}, \xi_h]$ (backward scheme), for $\xi_h = 1$, i.e. at j.

To be noted is that the definition of the coefficient for the two end quadrature cross-sections, i.e., $\xi_h = 0$ and $\xi_h = 1$, is required only for the first order derivative, to construct matrix $\boldsymbol{\Delta}^1$ that appears in Eq. (54). For matrices $\boldsymbol{\Delta}^2_c$ and $\boldsymbol{\Delta}^1_c$ in Eq. (50), the definition of the coefficients for the central quadrature cross-sections suffices.

For equally spaced quadrature cross-sections, having distance $\Delta \xi$, matrices $\boldsymbol{\Delta}^2$ and $\boldsymbol{\Delta}^1$ appearing in Eqs. (43) and (44) result as:

$$\boldsymbol{\Delta}^2 = \frac{1}{L^2 \Delta \xi^2} \begin{bmatrix} 1 & -2 & 1 & 0 & \dots & 0 & 0 & 0 \\ 1 & -2 & 1 & 0 & \dots & 0 & 0 & 0 \\ 0 & 1 & -2 & 1 & \dots & 0 & 0 & 0 \\ \vdots & \vdots & \vdots & \vdots & \ddots & \vdots & \vdots & \vdots \\ 0 & 0 & 0 & 0 & \dots & 1 & -2 & 1 \\ 0 & 0 & 0 & 0 & \dots & 1 & -2 & 1 \end{bmatrix} \quad \text{and} \quad \boldsymbol{\Delta}^1 = \frac{1}{L \Delta \xi} \begin{bmatrix} -\frac{3}{2} & 2 & -\frac{1}{2} & 0 & \dots & 0 & 0 & 0 \\ -\frac{1}{2} & 0 & \frac{1}{2} & 0 & \dots & 0 & 0 & 0 \\ 0 & -\frac{1}{2} & 0 & \frac{1}{2} & \dots & 0 & 0 & 0 \\ \vdots & \vdots & \vdots & \vdots & \ddots & \vdots & \vdots & \vdots \\ 0 & 0 & 0 & 0 & \dots & -\frac{1}{2} & 0 & \frac{1}{2} \\ 0 & 0 & 0 & 0 & \dots & \frac{1}{2} & -2 & \frac{3}{2} \end{bmatrix} \tag{62}$$

where, except for the first and last rows, the coefficients repeat along the main diagonal. This is not the case of non-uniform cross-section distributions. As an example, for $n = 7$ Gauss–Lobatto quadrature cross-sections, the same matrices (computed by means of the Fornberg algorithm) result as:
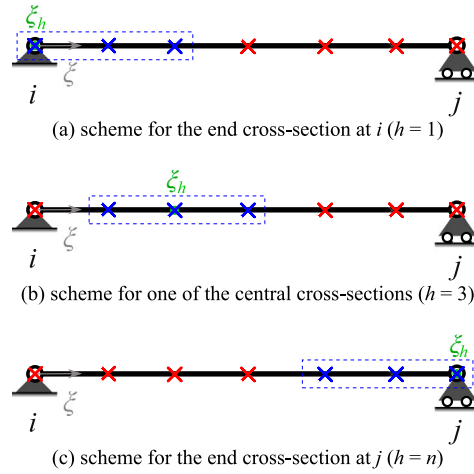
(a) scheme for the end cross-section at i ($h = 1$)

(b) scheme for one of the central cross-sections ($h = 3$)

(c) scheme for the end cross-section at j ($h = n$)

Fig. 6. Abscissas considered for the 3-point FD scheme, highlighting in blue those associated to non-zero coefficients (depicted for $n = 7$).

$$\Delta^2 = \frac{1}{L^2} \begin{bmatrix} \frac{8938}{403} & -\frac{3814}{117} & \frac{5512}{529} & 0 & 0 & 0 & 0 \\ \frac{8938}{403} & -\frac{3814}{117} & \frac{5512}{529} & 0 & 0 & 0 & 0 \\ 0 & \frac{4493}{674} & -\frac{3317}{281} & \frac{1079}{210} & 0 & 0 & 0 \\ 0 & 0 & \frac{3098}{681} & -\frac{5641}{620} & \frac{3098}{681} & 0 & 0 \\ 0 & 0 & 0 & \frac{1079}{210} & -\frac{3317}{281} & \frac{4493}{674} & 0 \\ 0 & 0 & 0 & 0 & \frac{5512}{529} & -\frac{3814}{117} & \frac{8938}{403} \\ 0 & 0 & 0 & 0 & \frac{5512}{529} & -\frac{3814}{117} & \frac{8938}{403} \end{bmatrix} \qquad (63)$$

$$\Delta^1 = \frac{1}{L} \begin{bmatrix} -\frac{4174}{537} & \frac{2779}{321} & -\frac{1233}{1394} & 0 & 0 & 0 & 0 \\ -\frac{541}{135} & \frac{559}{179} & \frac{1233}{1394} & 0 & 0 & 0 & 0 \\ 0 & -\frac{3202}{2049} & \frac{1046}{1649} & \frac{363}{391} & 0 & 0 & 0 \\ 0 & 0 & -\frac{947}{888} & 0 & \frac{947}{888} & 0 & 0 \\ 0 & 0 & 0 & -\frac{363}{391} & -\frac{1046}{1649} & \frac{3202}{2049} & 0 \\ 0 & 0 & 0 & 0 & -\frac{1233}{1394} & \frac{559}{179} & \frac{541}{135} \\ 0 & 0 & 0 & 0 & \frac{1233}{1394} & -\frac{2779}{321} & \frac{4174}{537} \end{bmatrix} \qquad (64)$$

For $n = 3$ Gauss–Lobatto quadrature cross-sections, the values coincides with those of the equally spaced case.

3.4.2. The 4-point scheme (FDDI4)

The 4-point scheme (hereafter indicated as FDDI4) constructs the FD approximation at the hth quadrature cross-section, i.e., at ξ_h, over 4 consecutive abscissas that always include ξ_h. Referring to Fig. 7, for the central quadrature cross-sections, two cases are distinguished:

- for those placed on the left of the mid-span, including eventual cross-sections located at mid-span, ($\xi_h \leq 0.5$), the scheme defines the order-3 Lagrange interpolant over the 4 consecutive abscissas $[\xi_{h-1}, \xi_h, \xi_{h+1}, \xi_{h+2}]$ (e.g., Fig. 7(b) depicted for the case $h = 3$), i.e., using an asymmetric forward-centered scheme;
- for those placed on the right of the mid-span ($\xi_h > 0.5$), the scheme defines the order-3 Lagrange interpolant over the 4 consecutive abscissas $[\xi_{h-2}, \xi_{h-1}, \xi_h, \xi_{h+1}]$ (e.g., Fig. 7(c) depicted for the case $h = 5$), i.e., using an asymmetric backward-centered scheme.

For the two end quadrature cross-sections (Fig. 7(a) and 7(d)), the scheme defines the order-3 Lagrange interpolant over the 4 consecutive abscissas $[\xi_h, \xi_{h+1}, \xi_{h+2}, \xi_{h+3}]$ (forward scheme), for $\xi_h = 0$, i.e. at i, and $[\xi_{h-3}, \xi_{h-2}, \xi_{h-1}, \xi_h]$ (backward scheme), for $\xi_h = 1$, i.e. at j.

(a) scheme for the end cross-section at i ($h = 1$)

(b) scheme for one of the central cross-sections ($h = 3$)

(c) scheme for one of the central cross-sections ($h = 5$)

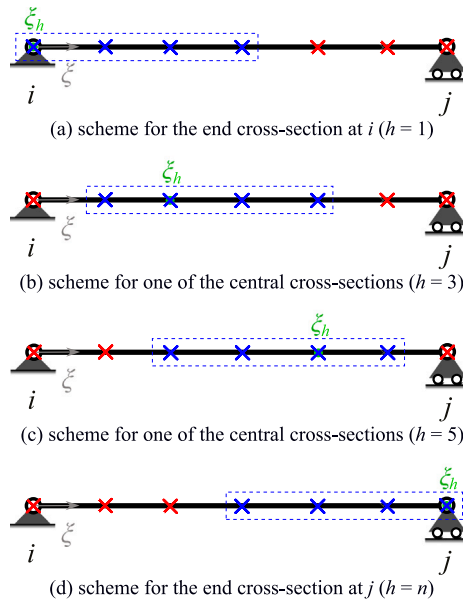(d) scheme for the end cross-section at j ($h = n$)

Fig. 7. Abscissas considered for the 4-point FD scheme, highlighting in blue those associated to non-zero coefficients (depicted for $n = 7$).

As an example, for $n = 4$ Gauss–Lobatto quadrature cross-sections, matrices $\boldsymbol{\Delta}^2$ and $\boldsymbol{\Delta}^1$ (computed by means of the Fornberg algorithm) result as:

$$
\boldsymbol{\Delta}^2 = \frac{1}{L^2}
\begin{bmatrix}
5 & -\frac{3170}{329} & \frac{3218}{451} & -\frac{5}{2} \\
\frac{963}{329} & -5 & \frac{5}{2} & -\frac{963}{2255} \\
-\frac{963}{2255} & \frac{5}{2} & -5 & \frac{963}{329} \\
-\frac{5}{2} & \frac{3218}{451} & -\frac{3170}{329} & 5
\end{bmatrix}
\quad \text{and} \quad
\boldsymbol{\Delta}^1 = \frac{1}{L}
\begin{bmatrix}
-3 & \frac{987}{244} & -\frac{2279}{1475} & \frac{1}{2} \\
-\frac{1292}{1597} & 0 & \frac{2889}{2584} & -\frac{305}{987} \\
\frac{305}{987} & -\frac{2889}{2584} & 0 & \frac{1292}{1597} \\
-\frac{1}{2} & \frac{2279}{1475} & -\frac{987}{244} & 3
\end{bmatrix}
\tag{65}
$$

3.4.3. The 5-point scheme (FDDI5)

The 5-point scheme (hereafter indicated as FDDI5) constructs the FD approximation at the hth quadrature cross-section, i.e., at ξ_h, over 5 consecutive abscissas that always include ξ_h. Referring to Fig. 8, when the considered h^{th} quadrature cross-section is a central one (e.g., Fig. 8(c) depicted for the case $h = 4$) the scheme defines the order-4 Lagrange interpolant over the 5 consecutive abscissas $[\xi_{h-2}, \xi_{h-1}, \xi_h, \xi_{h+1}, \xi_{h+2}]$ (centered scheme). Exception is made for the first and last central cross-sections (Fig. 8(b) and 8(d)). For them, the interpolant is constructed over the abscissas $[\xi_{h-1}, \xi_h, \xi_{h+1}, \xi_{h+2}, \xi_{h+3}]$ (asymmetric forward-centered scheme), for the first central cross-section ($h = 2$), and $[\xi_{h-3}, \xi_{h-2}, \xi_{h-1}, \xi_h, \xi_{h+1}]$ (asymmetric backward-centered scheme), for the last central cross-section ($h = n - 1$).

When the considered h^{th} quadrature cross-section is at the ends (Fig. 8(a) and 8(e)), the scheme defines the order-4 Lagrange interpolant over the 5 consecutive abscissas $[\xi_h, \xi_{h+1}, \xi_{h+2}, \xi_{h+3}, \xi_{h+4}]$ (forward scheme), for $\xi_h = 0$, i.e. at i, and $[\xi_{h-4}, \xi_{h-3}, \xi_{h-2}, \xi_{h-1}, \xi_h]$ (backward scheme), for $\xi_h = 1$, i.e. at j.

As an example, for $n = 5$ Gauss–Lobatto quadrature cross-sections, matrices $\boldsymbol{\Delta}^2$ and $\boldsymbol{\Delta}^1$ (computed by means of the Fornberg algorithm) result as:

$$
\boldsymbol{\Delta}^2 = \frac{1}{L^2}
\begin{bmatrix}
15 & -\frac{2673}{94} & \frac{64}{3} & -\frac{1748}{141} & \frac{9}{2} \\
\frac{3960}{551} & -\frac{35}{3} & \frac{16}{3} & -\frac{7}{6} & \frac{551}{1760} \\
-\frac{3}{4} & \frac{49}{12} & -\frac{20}{3} & \frac{49}{12} & -\frac{3}{4} \\
\frac{551}{1760} & -\frac{7}{6} & \frac{16}{3} & -\frac{35}{3} & \frac{3960}{551} \\
\frac{9}{2} & -\frac{1748}{141} & \frac{64}{3} & -\frac{2673}{94} & 15
\end{bmatrix}
\quad \text{and} \quad
\boldsymbol{\Delta}^1 = \frac{1}{L}
\begin{bmatrix}
-5 & \frac{2858}{423} & -\frac{8}{3} & \frac{777}{551} & -\frac{1}{2} \\
-\frac{551}{444} & 0 & \frac{1538}{881} & -\frac{1429}{1871} & \frac{769}{2969} \\
\frac{3}{8} & -\frac{274}{205} & 0 & \frac{274}{205} & -\frac{3}{8} \\
-\frac{769}{2969} & \frac{1429}{1871} & -\frac{1538}{881} & 0 & \frac{551}{444} \\
\frac{1}{2} & -\frac{777}{551} & \frac{8}{3} & -\frac{2858}{423} & 5
\end{bmatrix}
\tag{66}
$$

4. Preliminary analyses on the accuracy of the FDDI technique

Before evaluating the performance of the proposed beam FE model in reproducing the response of framed structures, the accuracy of the FDDI technique in describing the transverse displacements of a general element is examined. The simply supported 2D beam in Fig. 9, with length $L = 5\,\text{m}$ and cross-section dimensions $b = 0.3\,\text{m}$ and $h = 1\,\text{m}$, is considered as a reference case, since the force-based beam formulation (Section 2) computes the FE response in the local basic reference system and requires the cross-section
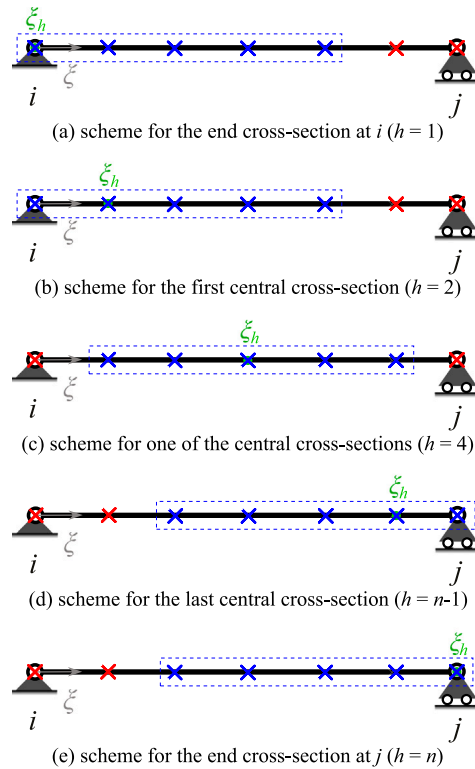
Fig. 8. Abscissas considered for the 5-point FD scheme, highlighting in blue those associated to non-zero coefficients (depicted for $n = 7$).
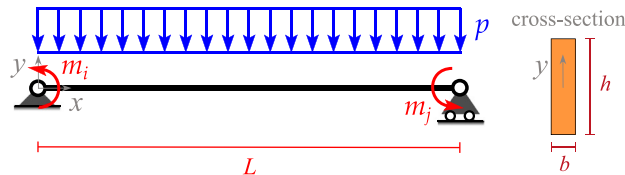

Fig. 9. Simply supported beam considered for the preliminary analyses.

transverse displacements with respect to a simply supported configuration. The beam is subjected to a uniform distributed load $p = 300\,\text{kN/m}$ and bending couples at the end nodes $m_i = 5000\,\text{kNm}$ and $m_j = 7000\,\text{kNm}$, which simulate the nodal couples m_{zi} and m_{zj} in the basic reference system (Fig. 1). Linear elastic material is assumed, with Young's modulus $E = 30\,\text{GPa}$ and Poisson ratio $v = 0.2$, and the shear correction coefficient is set equal to $\psi_y = 5/6$.

The goal of these preliminary analyses is to study the accuracy of the FDDI in determining the transverse displacements of the beam at selected cross-sections, under linear geometry. This permits assessing the efficiency of the technique, when used in the beam FE model, which requires the transverse displacement $v(x)$ and $w(x)$, at the quadrature cross-sections, for matrices $\mathbf{b}(x)$ and $\mathbf{b}^*(x)$ (Eqs. (12) and (14)). The computations are performed in Matlab.

Fig. 10 compares the transverse displacements $v(x)$ obtained by the FDDI3 (triangles), FDDI4 (squares), FDDI5 (crosses) and the CSBDI (circles) with the exact solution (dashed black curves). The latter is derived from the analytical integration of the bending curvature $\chi_z(x)$ and shear strain $\gamma_y(x)$ (Eq. (27)) and results in a variation of order 4 in x. The comparison is made for two different distributions of the n cross-sections along L: the Gauss–Lobatto quadrature scheme (a, c, e, g, i) and an equally spaced distribution (b, d, f, h, j). The number n varies from 3 (a, b) to 25 (i, j).

The FDDI5 gives the exact transverse displacements $v(x)$, since it has the highest order of accuracy. The FDDI4 and FDDI3 have lower orders of accuracy and, thus, show some solution errors. However, in general, the accuracy increases as n increases. Moreover, the FDDI4 practically gives the exact solution when 4 Gauss–Lobatto cross-sections are considered (Fig. 10(c)), which does not happen for $n > 4$ or for equally spaced cross-sections. On the contrary, the FDDI3 technique performs slightly better with equally spaced distributions than the Gauss–Lobatto one.
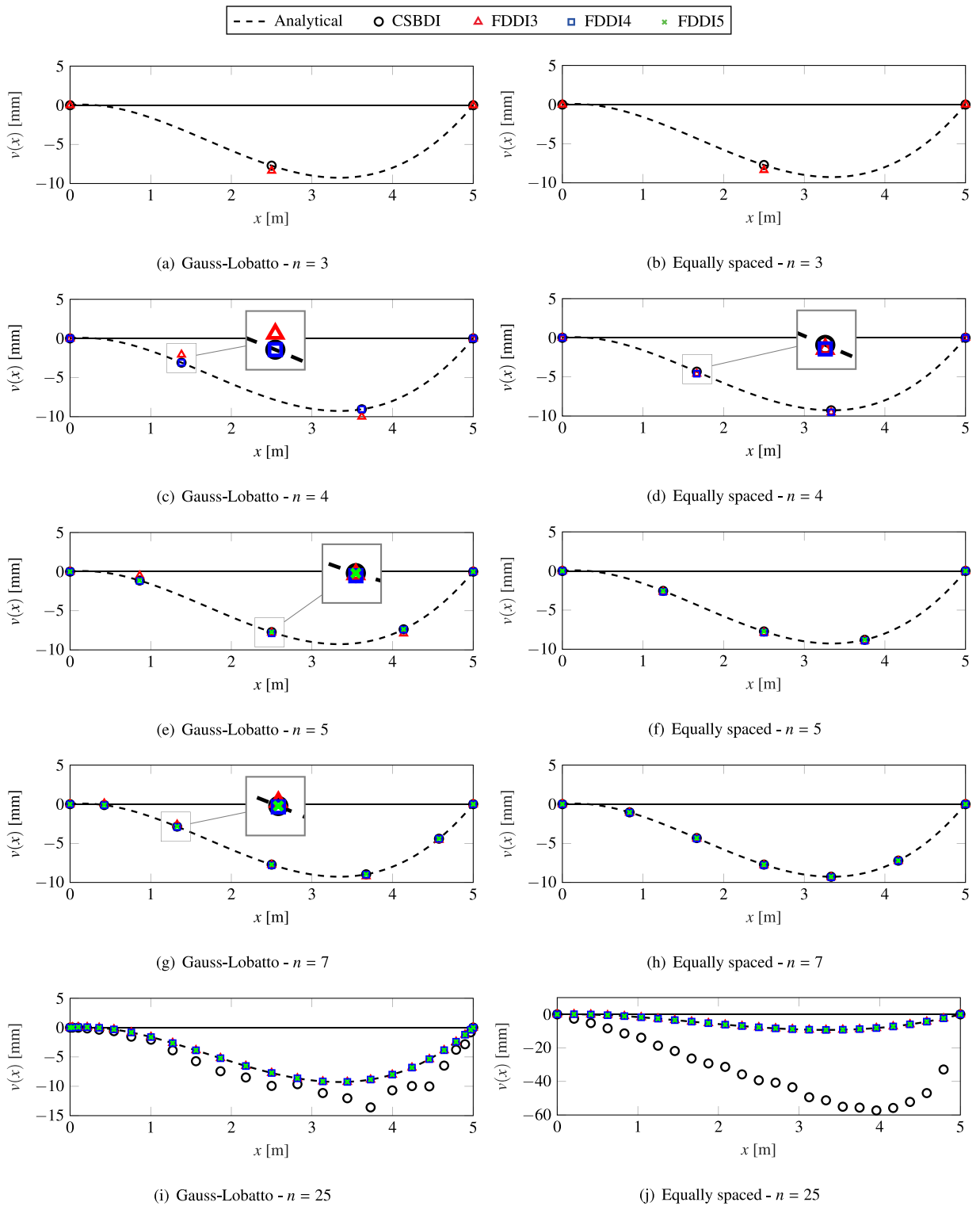
Fig. 10. Transverse displacements $v(x)$ of the simply supported beam for $p = 300\,\text{kN/m}$.

Similar simulations are performed for the same beam subjected only to the end couples, i.e., $p = 0$. For the Gauss–Lobatto distribution, the results are plotted in Fig. 11. In this case, the exact solution is cubic in x and thus both FDDI4 and FDDI5 are precise. The FDDI3 shows some errors that reduce as n increases, although, for $n = 3$, the solution is exact.
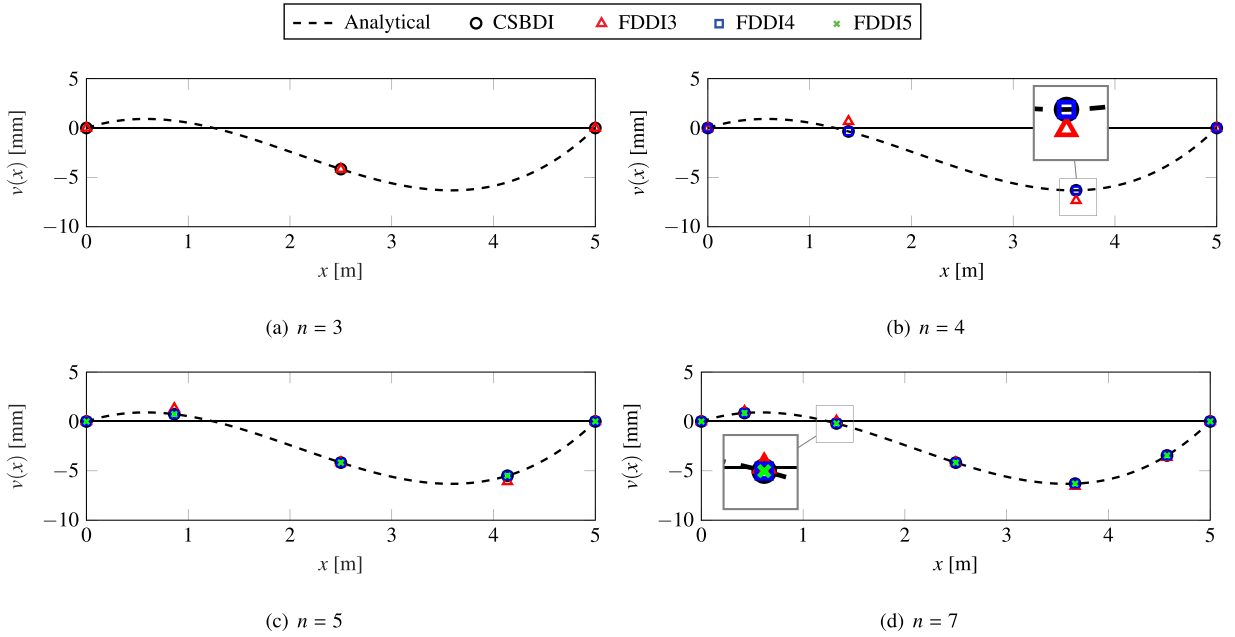
Fig. 11. Transverse displacements $v(x)$ of the simply supported beam for $p = 0$ — Gauss–Lobatto distributed cross-sections.

In all simulations, the CSBDI is very accurate. However, due to the ill-condition of matrix $\mathbf{G}$, when n increases, the accuracy reduces. For $n > 20$, the results deviate significantly from the exact values, as shown in Figs. 10(i) and 10(j) for $n = 25$. This issue can be mitigated and, thus, better solution can be computed if the inverse of matrix $\mathbf{G}$, in Eqs. (30) to (33), is evaluated as Moore–Penrose pseudoinverse (e.g., `pinv` command in Matlab) [61], or through enhanced algorithms, such as the LU or QR factorizations (e.g., *slash command* '/' in Matlab) [62].

For a more detailed description of the accuracy and convergence rate of the numerical models, Fig. 12 shows the variation of the average error $\bar{\mathcal{E}}$, obtained for the Gauss–Lobatto distribution for increasing n, when (a) $p = 300\,\text{kN/m}$ and (b) $p = 0$. The average error is defined as:

$$\bar{\mathcal{E}} = \frac{1}{L} \int_0^L |v(x)^{num} - v(x)|\, \mathrm{d}x \approx \frac{1}{L} \sum_{h=1}^{n} |v(x_h)^{num} - v(x_h)|\; w_h \tag{67}$$

where $v(x_h)^{num}$ is the numerical (FDDI or CSBDI) transverse displacement of the hth cross-section, $v(x_h)$ the corresponding exact analytical value, and w_h the associated Gauss–Lobatto quadrature weight. The plots confirm the observations made above on the accuracy of the FDDI technique (solid red, dashed blue, and solid green curves). For instance, the FDDI5 (solid green curves) always has an average error close to the machine precision. The plots also show the divergence of the CSBDI technique (solid black curves), which is avoided with the use of the LU or QR factorizations or the Moore–Penrose pseudoinverse (dashed black curves).

Given these results, in FE analyses, the following choices can be made, as done for all the numerical applications presented in the next Section:

- the FDDI3 ($p = 3$) can be used when $n = 3$;
- the FDDI4 ($p = 4$) can be used when $n = 4$;
- the FDDI5 ($p = 5$) can be used when $n \geq 5$.

The case $n = 5$, with $p = 5$, i.e., with the FDDI5, can usually be adopted, especially for frames subjected to distributed loads.

5. Numerical applications

The adopted beam FE model with both CSBDI and FDDI techniques is implemented in a standard FE code based on a step-by-step analysis and a Newton–Raphson (N–R) iterative scheme for the solution of nonlinear problems. The solution algorithm for determining the element state at each N–R iteration, i.e. to compute the nodal force vector $\mathbf{p}$ and stiffness matrix $\hat{\mathbf{k}}$ for a given set of nodal DOFs $\mathbf{u}$, is that proposed in [6] and reported in detail in Appendix A.

Two paradigmatic structures are numerically analyzed, considering both linear elastic and elasto-plastic material behaviors: the 2D Lee's frame [63] and a two-story 3D frame [64]. The performance of the adopted geometrically nonlinear beam formulation with moderately large deformations has been already studied in previous works, e.g. [6,42,44,47], where its high computational accuracy and efficiency is proved. Further investigation of this aspect is not the main the scope of this work, and thus the numerical
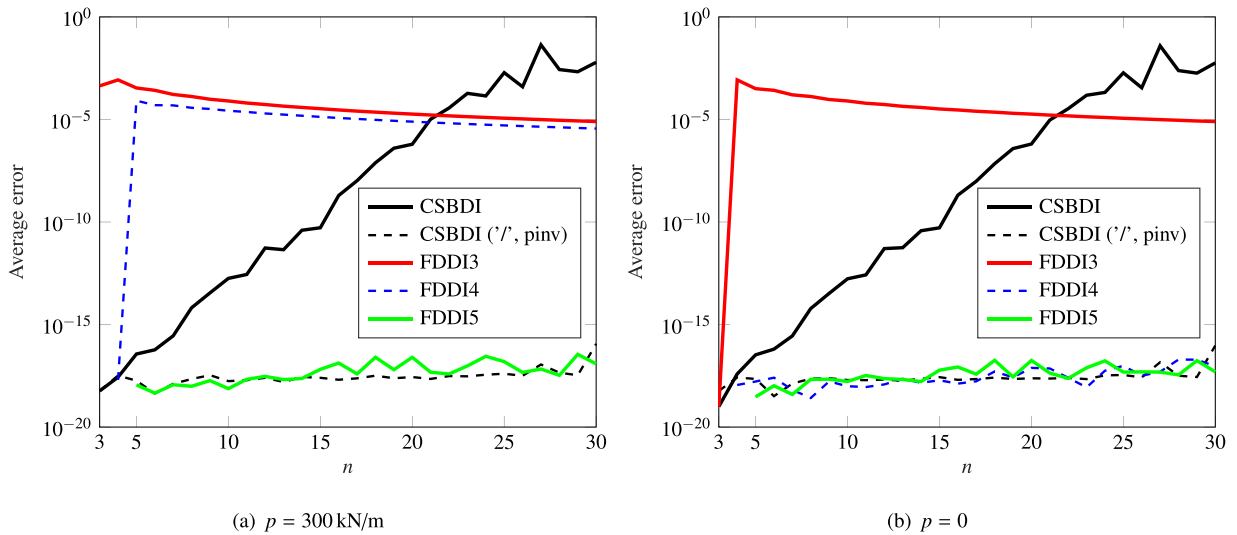
(a) $p = 300\,\text{kN/m}$

(b) $p = 0$

Fig. 12. Convergence rate for the transverse displacements $v(x)$ of the simply supported beam — Gauss–Lobatto distributed cross-sections.
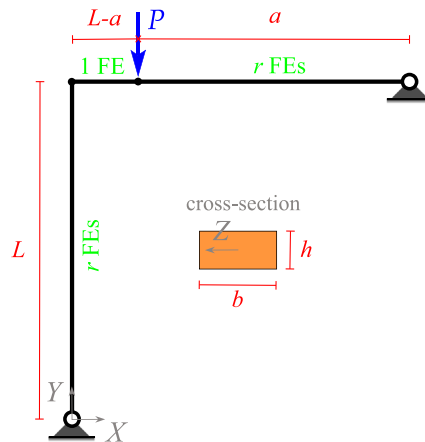

Fig. 13. Lee's frame: geometry and FE mesh.

applications primarily focus on the performance of the FDDI compared to the CSBDI technique. However, to give a wider perspective of the model performance, a third test is conducted, related to the analysis of a six-story 2D frame, where the response obtained with the proposed model is compared with a richer mixed beam formulation available in the literature.

To be noted is that, for all analyses performed with the CSBDI technique, to alleviate the numerical issues related to the ill-condition of matrix **G**, the QR factorization is used to compute the inverse of this matrix, but similar behavior can be also obtained with the LU factorization or the Moore–Penrose pseudoinverse.

Moreover, when elasto-plastic material is considered, to properly account for the stress coupling under constitutive nonlinearities, a fiber cross-section model [2] is used to perform the Section State Determination (Step 7 of Table 1 in Appendix A). The adopted fiber model is based on the Midpoint distribution, which in general is more accurate than other distributions [65–67].

5.1. Lee's frame

The first numerical application considers the 2D frame depicted in Fig. 13. Its response under linear elastic material was calculated analytically by Lee et al. [63] and obtained numerically by other authors, e.g. [1,3,15,68]. Cichon [69] and De Souza [6] also studied the behavior of the frame under elasto-plastic material, the former adopting a nonlinear beam model based on the Total Lagrange Approach, while the latter adopting the same beam formulation of this work, yet based on the Euler–Bernoulli theory and endowed with the CBDI technique, as the shear deformations are negligible in this test.

Fig. 13 also indicates the considered 2D beam–column FE mesh, where r FEs are used to model the column, while r FEs and 1 FE are used for the beam portion on the right- and left-hand sides of the applied load P, respectively. Frame dimensions are $L = 120\,\text{cm}$, $a = 96\,\text{cm}$, $b = 3\,\text{cm}$ and $h = 2\,\text{cm}$.

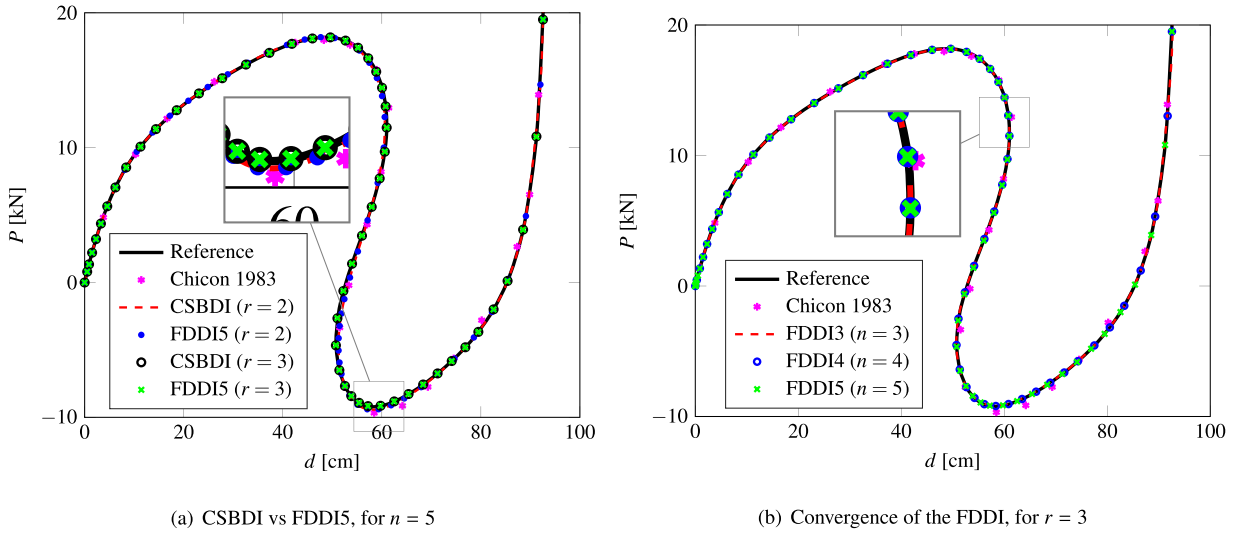(a) CSBDI vs FDDI5, for $n = 5$

(b) Convergence of the FDDI, for $r = 3$

Fig. 14. Response of the Lee's frame for linear elastic material.

For linear elastic material, Young's modulus $E = 70608$ MPa and Poisson ratio $\nu = 0.3$ are assumed. In addition to the Chicon's solution, a reference response is computed with standard force-based beam elements, that is, based on linear kinematic for the description of the intra-element deformations, but accounting for large displacements and rotations of the end nodes by means of the corotational formulation [6,23,24,47]. For this solution, an overkilling mesh is considered, made of 88 FEs, i.e., 40 FEs for the column and 48 FEs for the beam, with 8 FEs on the left-hand side of the load (on the length $L-a$). The cross-section shear correction coefficient is assumed equal to $\psi_y = 5/6$.

De Souza [6] showed that, when using the adopted beam formulations with moderately large deformations, 1 FE per member, i.e., $r = 1$, is not sufficient to obtain a correct solution. Thus, in the following, the meshes with $r = 2$ and $r = 3$ are used, and the response accuracy is studied by varying the number n of quadrature cross-sections placed in each FE. These always follow the Gauss–Lobatto scheme. For all the analyses, an arc-length method is used to obtain the global equilibrium path.

Fig. 14(a) plots the frame response curve in terms of applied load P versus vertical displacement d of the loaded point, showing that the structure undergoes severe nonlinear geometric effects, resulting in a snap-back behavior. For $n = 5$, the CSBDI (red dashed curve and black circles) and FDDI5 (blue dots and green crosses) practically give the same solution. For the mesh with $r = 2$, this solution deviates very slightly from the reference, while perfect matching results for $r = 3$.

The influence of the FD scheme used in the FDDI technique is explored in Fig. 14(b). This shows the solutions obtained with the mesh where $r = 3$, for the FDDI3 with $n = 3$ (dashed red curve), FDDI4 with $n = 4$ (blue circles), and FDDI5 with $n = 5$ (green crosses). All of these overlap with the reference solution, confirming the results observed in the preliminary analyses (Section 4), i.e., for linear elastic material behavior, in the absence of distributed loads, the FDDI4 and FDDI5 are always accurate, while the FDDI3 results accurate for $n = 3$.

A deeper investigation of the accuracy of the FDDI technique is made for the case of elasto-plastic material. Yield stress is assumed equal to $\sigma_y = 1020$ MPa, and linear kinematic hardening is considered, with plastic hardening modulus $E_H = 0.1 E$. The cross-section fiber discretization adopts 10 Midpoint fibers along the depth h and 5 Gauss–Lobatto quadrature cross-sections are used in the reference solution obtained with the overkilling mesh.

Fig. 15 shows the response, using the same representation and curve style as the linear elastic results in Fig. 14. Similar observations also hold, except that, in this case, the FDDI with $n = 3$ (red dashed curve in Fig. 15(b)) is slightly less precise, while the FDDI4 and FDDI5 always give very accurate solutions.

Fig. 16(a) shows the deformed configurations of the frame for $d = 30$ cm, 60 cm and 85 cm. These are depicted for the reference model (black solid curves), the CSBDI (red dashed curves), and the FDDI5 (blue dashed curves). For these latter, the cases $r = 3$ and $n = 5$ are considered, which gives accurate results, with negligible error.

For a more detailed evaluation of the numerical error, for the case of elasto-plastic material, the convergence rate of the CSBDI and FDDI techniques is studied when the number n of quadrature cross-sections per beam increases. The accuracy of the solution is defined in terms of the average error $\bar{\mathcal{E}}_p$, computed as:

$$\bar{\mathcal{E}}_p = \frac{1}{d_{max}} \int_0^{d_{max}} \left| P - P^{ref} \right| \, \mathrm{d}d \tag{68}$$

where $\left| P - P^{ref} \right|$ indicates the absolute difference in terms of load between the analyzed and reference solutions, while $[0; d_{max} = 89$ cm$]$ is the displacement interval where this difference is evaluated.

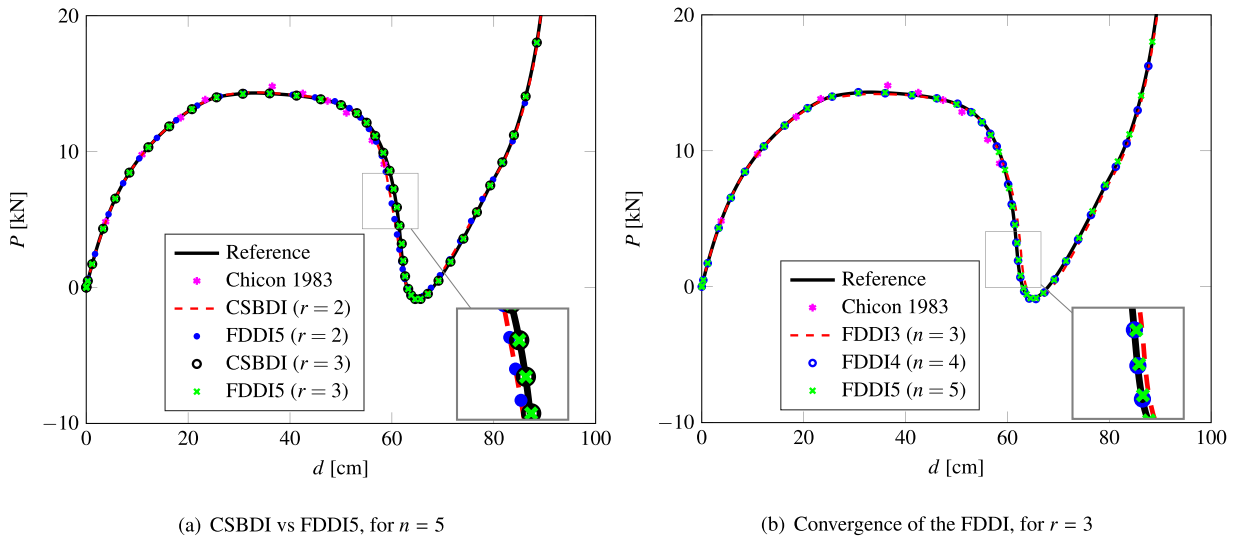(a) CSBDI vs FDDI5, for $n = 5$

(b) Convergence of the FDDI, for $r = 3$

Fig. 15. Response of the Lee's frame for elasto-plastic material.

(a) Deformed shape (scale factor = 1)
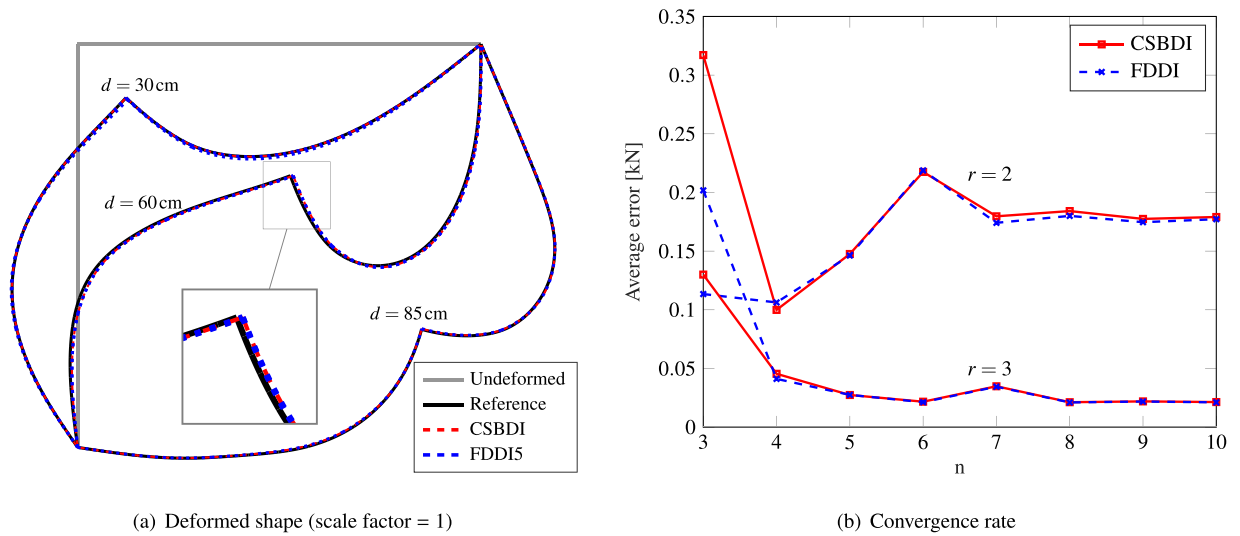
(b) Convergence rate

Fig. 16. Response of the Lee's frame obtained with the adopted beam formulation for elasto-plastic material.

Fig. 16(b) plots the variation of $\bar{\mathcal{E}}_p$ for the CSBDI (solid red curves with squares) and FDDI (dashed blue curves with crosses) obtained for the FE mesh with $r = 2$ and 3. The FDDI always uses the 5-point scheme (FDDI5), except for $n = 3$ and 4, where the FDDI3 and FDDI4 are adopted, respectively.

The figure shows that the two techniques practically have the same level of accuracy (except for $n = 3$), which, as expected, improves when the mesh is refined. However, oscillatory behavior is observed when n increases, due to the way the model describes the spread of plasticity. In fact, for different values of n, different quadrature cross-section positions are considered along the elements, as, in each FE, the Gauss–Lobatto quadrature scheme places the central cross-sections differently depending on whether n is odd or even. As example, Fig. 17 plots the positions of the quadrature cross-sections (red crosses) in the CSBDI and FDDI models for (a) $r = 2$ and (b) $r = 3$, and compares them with the distribution of the plastic zones resulting from the reference model, at $d = 60$ cm. However, the oscillations of the average error mitigate as r increases.

5.2. Two-story 3D frame

The second numerical application reproduces the response of the elasto-plastic two-story 3D frame in Fig. 18. This was studied by Argyris et al. [64], Abbasnia and Kassimali [70], and Rezaiee-Pajand and Gharaei-Moghaddam [44], adopting nonlinear beam numerical approaches. The latter use the same beam formulation of this work, endowed with the CSBDI technique.
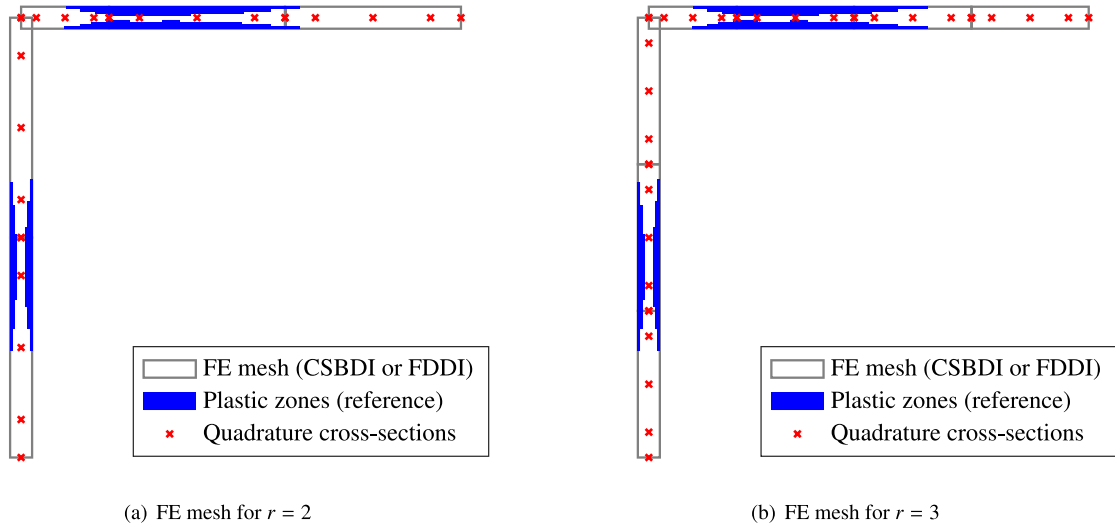
(a) FE mesh for $r = 2$

(b) FE mesh for $r = 3$

Fig. 17. Plastic zone distribution obtained from the reference model at $d = 60$ cm, compared with the location of the Gauss–Lobatto quadrature cross-sections in the CSBDI and FDDI models (in the extruded FE mesh, cross-section depth is scaled by a factor 3, for a clearer representation).
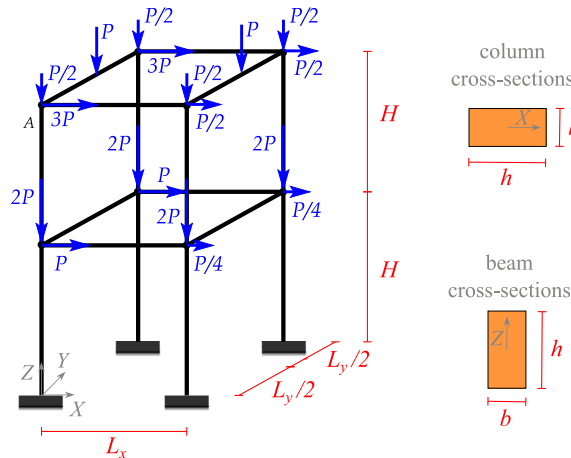

Fig. 18. Two-story 3D frame: geometry and loading configuration.

The frame dimensions are $L_x = 4$ m, $L_y = 3$ m, $H = 4$ m, $b = 0.2$ m, $h = 0.4$ m, while elastic perfectly plastic material is assumed with Young's modulus, Poisson ratio and yield stress equal to $E = 19613$ MPa, $\nu = 0.17$ and $\sigma_y = 98$ MPa, respectively.

Due to the symmetry, only half of the frame is modeled, with a uniform mesh that places r FEs for each structural member. The cross-section fiber discretization considers a Midpoint grid of 4×8 fibers along the dimensions b and h, respectively. The cross-section correction coefficients are assumed equal to $\psi_y = \psi_z = 5/6$ and $\psi_x = 0.3$. Moreover, to avoid numerical convergence issues due to the assumption of elastic perfectly plastic material, linear kinematic hardening is included, yet setting a very low value of the plastic hardening modulus ($E_H = 0.00001 \, E$).

Fig. 19(a) shows the relationship between the reference applied load P and the horizontal displacement u_A of the top node A along the X direction for the frame. The curve exhibits a linear elastic behavior at first, followed by a nonlinear plastic behavior after the formation of plastic hinges at the ends of the beams parallel to X and of the column [64]. In this work, the computation is extended to a higher value of the maximum displacement than in [64], which was almost 0.62 m, to better investigate the effect of the geometric nonlinearities.

The figure shows the reference solution (black solid curve) obtained by using standard force-based beam elements with linear intra-element deformations and the corotational formulation from [47,48] to account for the large nodal displacements and rotations. This considers a very fine mesh with $r = 20$. Moreover, the figure compares the solutions obtained by the CSBDI (red dashed curve and black circles) and FDDI5 (blue dots and green crosses) techniques for FE meshes with $r = 1$ and 2, and adopting $n = 5$. These practically give the same results that very well agree with the reference one. The response from [64] (magenta asterisk) is included for comparison.
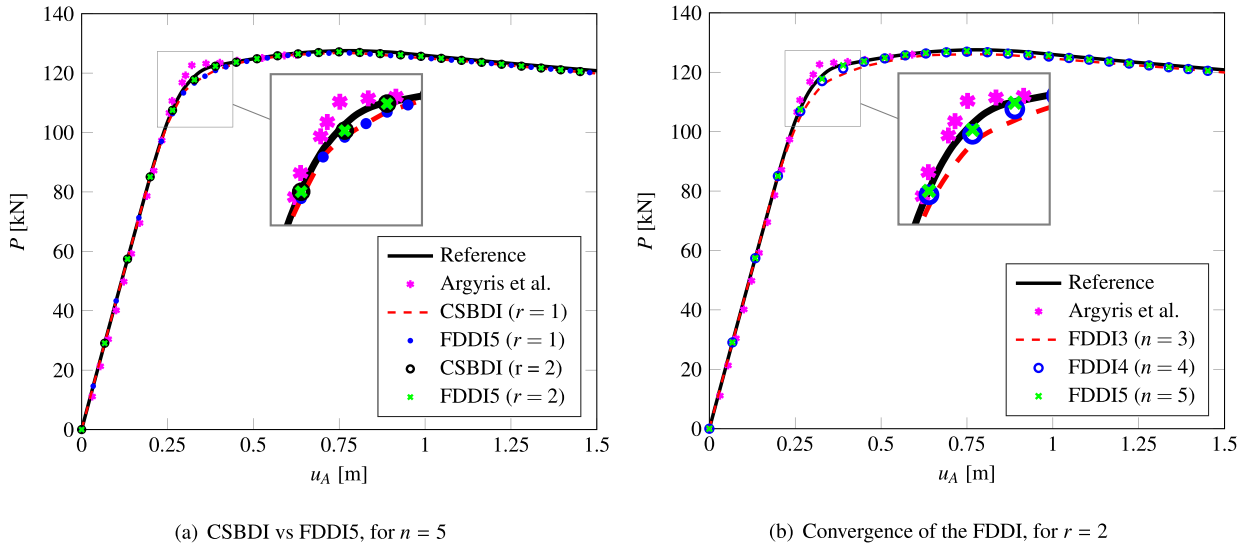
(a) CSBDI vs FDDI5, for $n = 5$

(b) Convergence of the FDDI, for $r = 2$

Fig. 19. Response of the elasto-plastic two-story 3D frame.

(a) Deformed shape at $u_A = 1.5$ m
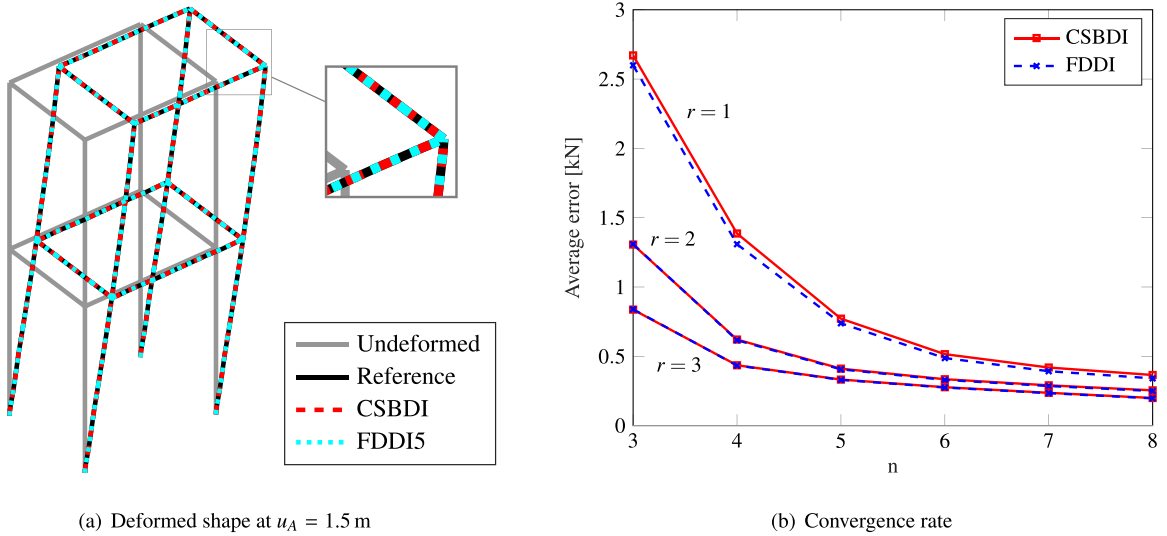
(b) Convergence rate

Fig. 20. Response of the elasto-plastic two-story 3D frame obtained with the adopted beam formulation.

The influence of the FD scheme used in the FDDI technique is explored in Fig. 19(b), considering the FE mesh where $r = 2$. Although very similar results are obtained for the FDDI3 ($n = 3$, dashed red curve), FDDI4 ($n = 4$, blue circles) and FDDI5 ($n = 5$, green crosses), the comparison shows that the FDDI5 performs slightly better, in particular at the transition from the elastic to the plastic regime.

It is worth noting that both the CSBDI and FDDI techniques exhibit similar computational costs. To compare their performance in this regard, the analysis with $r = 2$ and $n = 5$ was conducted 200 times with both models, while measuring CPU time (Matlab R2023b code running on personal computer equipped with a Intel Core i7-1165G7 @ 2.80 GHz processor and 16 GB of RAM). The average execution time for a single analysis is found to be almost 203 s and 200 s, for the CSBDI and FDDI model, respectively.

Additional comparison is made in terms of the deformed configurations shown in Fig. 20(a) for $u_A = 1.5$ m. The configurations depicted for the CSBDI (red dashed curves) and FDDI5 (cyan dashed curves), for $r = 2$ and $n = 5$, perfectly match and coincide with the reference result (black solid curves).

Finally, Fig. 20(b) shows the rate of convergence to the reference solution of the CSBDI (solid red curves with squares) and FDDI (dashed blue curves with crosses), when the number n of quadrature cross-sections increases. The accuracy is defined in terms of the average error $\bar{\mathcal{E}}_p$, computed as in Eq. (68), with $d_{max} = 1.5$ m. The FDDI always uses the 5-point scheme (FDDI5), except for $n = 3$ and 4, where the FDDI3 and FDDI4 are adopted, respectively.
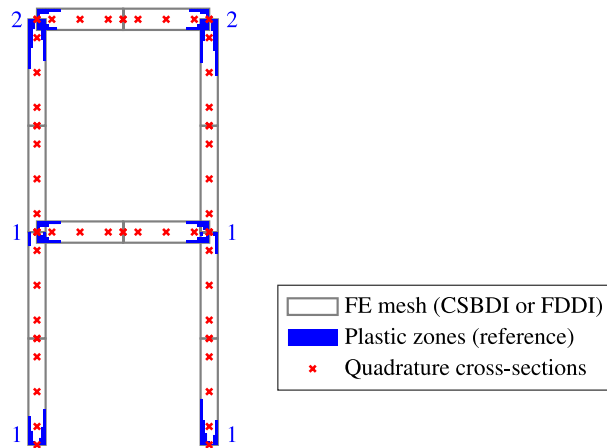
Fig. 21. Plastic zone distribution obtained from the reference model at $u_A = 1.5\,\text{m}$, compared with the location of the Gauss–Lobatto quadrature cross-sections in the CSBDI and FDDI models.

As observed for the Lee's frame, the two techniques practically have the same level of accuracy, which improves when the mesh is refined. The FDDI performs slightly better for coarser meshes ($r = 1$). However, as opposed to the Lee's frame, monotonic convergence is obtained in this case, as plasticity occurs at the beam ends. The distribution of the plastic zones (plastic hinges) resulting from the reference model, at $u_A = 1.5$ m, is plotted in Fig. 21, which includes only the beams and columns in the X–Y plane, as the transverse beams do not exhibit yielding. The plastic hinges labeled as 1 forms first, almost at the same loading step, followed by those labeled as 2. The figure also shows the positions of the quadrature cross-sections (red crosses) in the CSBDI and FDDI models.

5.3. Six-story 2D frame

The third test considers the six-story 2D frame represented in Fig. 22, with the main goal of comparing the proposed model performance with that of other beam formulations.

Indeed, the frame has been analyzed by Magisano et al. [40] adopting both a displacement-based and mixed beam finite element model. The former uses a quadratic Lagrangian displacement interpolation, improved with an enhanced assumed strain definition to prevent shear-locking, while the latter, in addition to the cross-section displacement expansion, independently interpolates the beam internal forces from nodal variables. For both models, a geometrically exact kinematics is assumed [8,50].

Fig. 22 also shows the vertical distributed loads and the horizontal concentrated forces acting on the frame. In the numerical analysis, these are simultaneously amplified by a load multiplier.

Frame dimensions are $L = 4$ m, $H = 3.75$ m, and an elastic perfectly plastic material is assumed with Young's modulus, Poisson ratio and yield stress equal to $E = 205000$ MPa, $v = 0.3$ and $\sigma_y = 235$ MPa, respectively.

The numerical simulations performed with the adopted beam model with moderately large deformations consider only the FDDI technique, with r equally-spaced FEs for each structural members. The I-shaped cross-sections are discretized into Midpoint layers, with 2 layers across each flange thickness and 6 layers along the web. The shear correction coefficient ψ_y is assumed equal to the ratio between the area of the web and the total area of the cross-section. Moreover, to avoid numerical convergence issues due to the assumption of elastic perfectly plastic material, linear kinematic hardening is included, yet setting a very low value of the plastic hardening modulus ($E_H = 0.00001\,E$).

Fig. 23(a) plots the frame response in terms of load multiplier versus horizontal displacement of the top left joint, comparing the performance of the proposed model, endowed with a FDDI5 scheme with $n = 5$ Gauss–Lobatto cross-sections, and that of the mixed beam formulation in [40], resulting more efficient than the displacement-based approach. Notably, the mixed model in [40] yields a sufficiently precise solution utilizing 2 FEs per structural member (green solid curve). For enhanced accuracy, a solution employing 8 mixed FEs is also illustrated (black dashed curve).

Despite the less accurate kinematic definition, the FDDI-based model shows similar performance. A good solution is already obtained with $r = 1$ (black dotted cuve), although improvement is observed for $r = 2$ (red crosses) and $r = 3$ (blue solid curve). This achievement is primarily attributed to the use of the corotational formulation, which inherently captures a significant part of the nonlinear contribution.

Fig. 23(b) examines the impact of the FD scheme implemented for the FDDI technique, specifically for the scenario where $r = 3$. In light of the initial findings presented in Section 4, the analysis is limited to schemes where $n > 4$, that are practically equivalent in terms of the results.

Ultimately, as done for the two-story 3D frame test, to compare the performance of the FDDI and CSBDI in terms of computational burden, the analysis with $r = 3$ and $n = 5$ is conducted 200 times with both techniques, while measuring CPU time (Matlab R2023b code running on personal computer equipped with a Intel Core i7-1165G7 @ 2.80 GHz processor and 16 GB of RAM). The average execution time for a single analysis is found to be almost 225 s and 226 s, for the CSBDI and FDDI model, respectively.
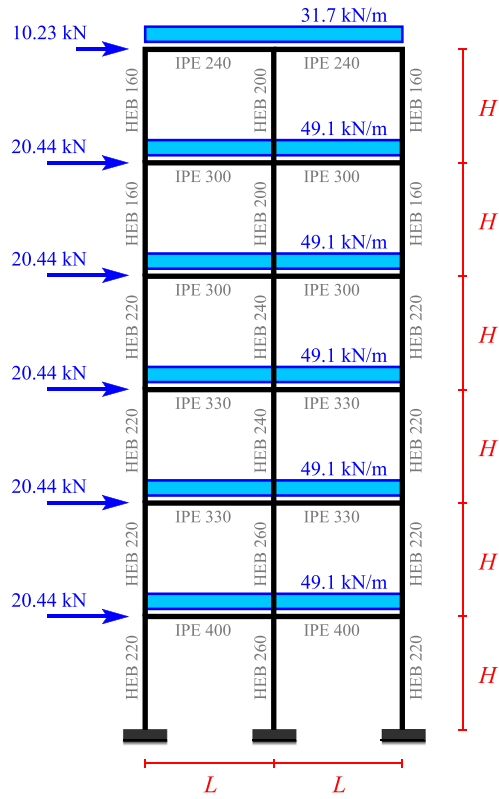
Fig. 22. Six-story 2D frame: geometry and loading configuration.
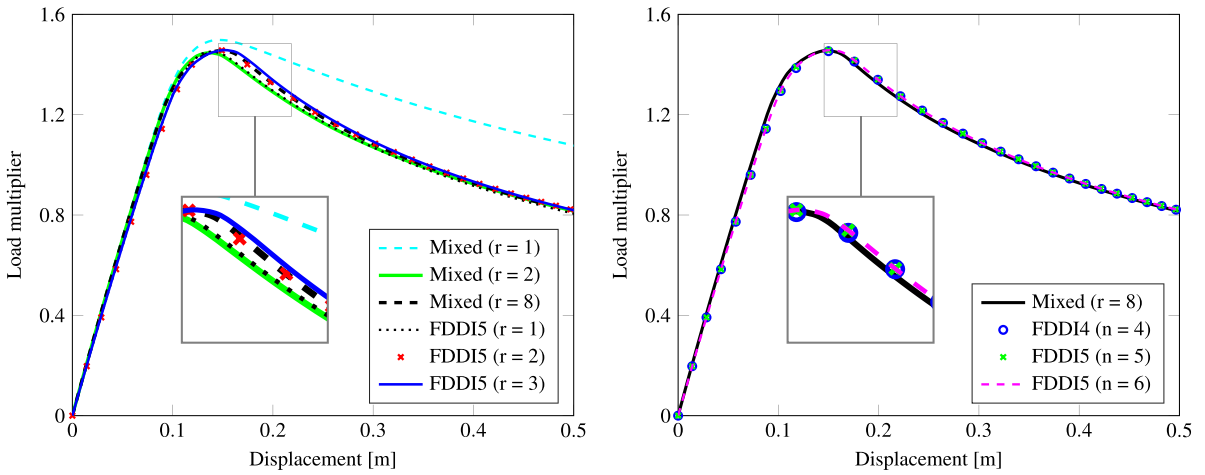
(a) Convergence of the FDDI, for $n = 5$

(b) Convergence of the FDDI, for $r = 3$

Fig. 23. Response of the elasto-plastic six-story 2D frame.

6. Conclusions

This work proposed a novel technique, called FDDI, for computing the transverse displacements in force-based beam FEs. The FDDI is based on the finite difference approximation of the cross-section compatibility conditions and is especially useful for geometrically nonlinear frame analysis. The technique is introduced in the enhanced force-based beam model with moderately large deformations, as an alternative to the CSBDI.

The FDDI can use many FD schemes to compute the quadrature cross-section displacements, as long as the two end quadrature cross-sections are included, which is usual in nonlinear beam simulations. Moreover, using Fornberg algorithm, the technique easily applies to quadrature rules with non-uniform cross-section distributions.

This work presented three fundamental FDDI schemes with 3, 4, and 5 points (FDDI3, FDDI4, and FDDI5), and explained their implementation details. Their performance were compared with that of the CSBDI, using numerical simulations of linear and nonlinear geometric and material behavior of representative specimens.

Silvaselvan et al. [37] noted that the Lagrange interpolation of CSBDI may induce displacement oscillations when more quadrature cross-sections are employed, leading to a loss of accuracy. In this work, the ill-conditioning of the CSBDI governing matrices was also discussed and the impact of these issues was investigated through specific preliminary tests, presented in Section 4, and the analysis of typical structures, reported in Section 5.

The CSBDI performs well in standard cases. However, the numerical tests revealed that the FDDI is a valuable alternative, as this consistently maintains an accuracy level at least equal to the CSBDI, while circumventing numerical challenges associated with matrix ill-conditioning and potential displacement oscillation. This advantage holds true even when considering a high number n of quadrature cross-sections. In any case, the FDDI demonstrates enhanced robustness compared to the CSBDI, which is more prone to convergence difficulties.

On the other hand, the FDDI offers computational efficiency comparable to that of the CSBDI and the relationship between cross-section generalized strains and displacements (Eqs. (21) and (22)) are expressed in similar fashion. This allows to preserve the architecture of the finite element formulation and solution algorithm, without affecting the computational time required for the analysis. Hence, the FDDI showed promise in geometrically nonlinear structural analysis, as well as post-processing purposes.

For elements without distributed loads, the 4- and 5-point schemes (FDDI4 and FDDI5) are very accurate, but only the FDDI5 can handle distributed loads accurately, as shown by the very common case of uniform loads considered in this work. The 3-point scheme (FDDI3) is less accurate and works well only when 3 quadrature cross-sections are used along the FE length. Therefore, the following criteria are suggested in practice: the adoption of the FDDI3 when $n = 3$, of the FDDI4 when $n = 4$, and of the FDDI5 for any other case ($n \geq 5$). The FDDI5 with $n = 5$ is usually the best choice for balancing accuracy and computational cost. However, increasing n improves the results.

CRediT authorship contribution statement

Paolo Di Re: Writing – review & editing, Writing – original draft, Visualization, Validation, Supervision, Software, Methodology, Investigation, Formal analysis, Data curation, Conceptualization. **Daniel Macabeo Benaim Sanchez:** Validation, Software, Investigation, Formal analysis, Supervision.

Declaration of competing interest

The authors declare that they have no known competing financial interests or personal relationships that could have appeared to influence the work reported in this paper.

Data availability

The authors have shared the link to the repository that contains the data

Digital data for "Finite difference technique for the evaluation of the transverse displacements in force-based beam finite elements" (Original data) (Mendeley Data).

Appendix A. Element solution algorithm

During the general N–R iteration, the displacements and rotations $\mathbf{u}$ of the element nodes i and j, in the global reference system (nodal DOFs), are given and, accordingly, the global nodal force vector $\mathbf{p}$ and the stiffness matrix $\hat{\mathbf{k}}$ are calculated (Element State Determination) and assembled. As usual in force-based and mixed beam FEs, internal element iterations are required to impose the compatibility of the nodal basic displacements $\mathbf{u}$ with the basic deformation displacements $\mathbf{v}$ of the element [2,4,26]. Hence, a specific algorithm is used to solve the Element State Determination of the adopted beam model. This is summarized in Table 1, referring to the evaluation of the FE response during an N–R iteration of a general loading step. The superscripts 'k' and '$k + 1$' denote the previous and current N–R iterations, respectively, while Δ denotes the increment with respect to the previous iteration.

For the proposed element, internal iterations are defined based on the following incremental form of the generalized cross-section constitutive law that considers the coupled behavior between cross-sections due to the adoption of numerical techniques CSBDI or FDDI for the computation of transverse displacements [6]. Indeed, it results:

$$\delta \mathbf{E} = \left(\mathbf{K}_s - \mathbf{K}_{sH} \right)^{-1} \delta \mathbf{S} \tag{69}$$

Table 1
Element state determination

(1)	$\mathbf{u}^{k+1}$ and $\Delta\mathbf{u}^{k+1}$ are given	
(2)	$\mathbf{v}^{k+1}$, $\Delta\mathbf{v}^{k+1}$ and $\mathbf{a}_g^{k+1}$ (kinematic matrix) are obtained from corotational formulation	see Refs. [47,48]
(3)	$\Delta\mathbf{q}^{k+1} = \left(\mathbf{f}^k\right)^{-1}\mathbf{a}_g\,\Delta\mathbf{u}^{k+1}\qquad\rightarrow\qquad \mathbf{q}^{k+1} = \mathbf{q}^k + \Delta\mathbf{q}^{k+1}$	
	Element internal iterations: Set counter $l=0$, element state at $l=0$ is set equal to that at k, and $\mathbf{q}^1 = \mathbf{q}^{k+1}$	
(4)	Recover $\mathbf{V}^l$, $\mathbf{V}'^l$, $\mathbf{W}^l$ and $\mathbf{W}'^l$ to compute $\mathbf{b}^l$	[Eq. (12)]
(5)	$\bar{\mathbf{s}}^{l+1} = \mathbf{b}^l\,\mathbf{q}^{l+1} + \mathbf{s}_b^{l+1} - \mathbf{s}^l\qquad\rightarrow\qquad \bar{\mathbf{S}}^{l+1} = \left\{\bar{\mathbf{s}}_1^{l+1^T}\quad\cdots\quad\bar{\mathbf{s}}_n^{l+1^T}\right\}^T$	[Eq. (11)]
(6)	$\Delta\mathbf{E}^{l+1} = \left(\mathbf{K}_s^l - \mathbf{K}_{sH}^{l+1}\right)^{-1}\bar{\mathbf{S}}^{l+1}\qquad\rightarrow\qquad \mathbf{e}^{l+1} = \mathbf{e}^l + \Delta\mathbf{e}^{l+1}$	[Eq. (69)]
(7)	Section State Determination: $\quad\mathbf{e}^{l+1}\quad\rightarrow\quad\mathbf{s}^{l+1}\quad$ and $\quad\mathbf{k}_s^{l+1}$	[Section 2.1]
(8)	Update $\mathbf{V}^{l+1}$, $\mathbf{V}'^{l+1}$, $\mathbf{W}^{l+1}$ and $\mathbf{W}'^{l+1}$	[Eqs. (21) and (22)]
(9)	Compute $\mathbf{b}^{l+1}$	[Eq. (12)]
(10)	$\bar{\mathbf{s}}^{l+1} = \mathbf{b}^{l+1}\,\mathbf{q}^{l+1} + \mathbf{s}_b^{l+1} - \mathbf{s}^{l+1}\qquad\rightarrow\qquad \bar{\mathbf{S}}^{l+1} = \left\{\bar{\mathbf{s}}_1^{l+1^T}\quad\cdots\quad\bar{\mathbf{s}}_n^{l+1^T}\right\}^T$	[Eq. (11)]
(11)	$\Delta\mathbf{E}^{l+1} = \left(\mathbf{K}_s^{l+1} - \mathbf{K}_{sH}^{l+1}\right)^{-1}\bar{\mathbf{S}}^{l+1}\qquad\rightarrow\qquad \mathbf{e}^{l+1} = \mathbf{e}^l + \Delta\mathbf{e}^{l+1}$	[Eq. (69)]
(12)	Update $\mathbf{b}^{l+1}$ and compute $\mathbf{b}^{*l+1}$	[Eqs. (12)] and Ref. [47]
(13)	$\mathbf{s}^{l+1} = \mathbf{b}^{l+1}\,\mathbf{q}^{l+1} + \mathbf{s}_b^{l+1}$	[Eq. (11)]
(14)	Compute $\mathbf{r}^{l+1}$ and $\mathbf{g}^{l+1}$ at quadrature points	see Refs. [47,48]
(15)	$\mathbf{f}^{l+1} = \sum_{h=1}^n\left\{\mathbf{b}^{*l+1^T}(\xi_h)\,\mathbf{f}_s^{l+1}(\xi_h)\left[\mathbf{b}^{l+1}(\xi_h) + \mathbf{r}^{l+1}(\xi_h)\right] + \mathbf{g}^{l+1}(\xi_h)\right\}w_h$	[Eq. (16)$_2$]
(16)	$\bar{\mathbf{v}}^{l+1} = \mathbf{v}^{k+1} - \sum_{h=1}^n\mathbf{b}^{*l+1^T}(\xi_h)\,\mathbf{e}^{l+1}(\xi_h)\,w_h$	[Eq. (16)$_1$]
(17)	$\Delta\mathbf{q}^{l+1} = \left(\mathbf{f}^{l+1}\right)^{-1}\bar{\mathbf{v}}^{l+1}\qquad\rightarrow\qquad \mathbf{q}^{l+1} = \mathbf{q}^{l+1} + \Delta\mathbf{q}^{l+1}$	
(18)	If $\|\bar{\mathbf{v}}^{l+1}\| < tol.$ or $l+1 \geq I_{l\,max}\qquad\rightarrow\qquad$ Exit otherwise $l = l+1$, element state at $k+1$ is set equal to that at $l+1$, and go to step 4	
(21)	$\mathbf{p}^{k+1} = \mathbf{a}_g^{k+1^T}\,\mathbf{q}^{k+1} + \mathbf{p}_b^{k+1}$	see Refs. [47,48]
(22)	$\hat{\mathbf{k}}^{k+1} = \mathbf{a}_g^{k+1^T}\left(\mathbf{f}^{k+1}\right)^{-1}\mathbf{a}_g^{k+1} + \mathbf{k}_g^{k+1}$	see Refs. [47,48]

where $\mathbf{E}$ and $\mathbf{S}$ collect the strains and stresses, respectively, of all quadrature cross-sections, i.e.:

$$\mathbf{E} = \left\{\mathbf{e}_1^T\quad\cdots\quad\mathbf{e}_n^T\right\}^T \qquad\text{and}\qquad \mathbf{S} = \left\{\mathbf{s}_1^T\quad\cdots\quad\mathbf{s}_n^T\right\}^T \tag{70}$$

while $\mathbf{K}_s$ and $\mathbf{K}_{sH}$ are matrices assembled as:

$$\mathbf{K}_s = \begin{bmatrix}\mathbf{k}_{s\,1} & \cdots & \mathbf{0}\\ \vdots & \ddots & \vdots\\ \mathbf{0} & \cdots & \mathbf{k}_{s\,2}\end{bmatrix} \qquad\text{and}\qquad \mathbf{K}_{sH} = \begin{bmatrix}\mathbf{k}_{sH\,11} & \cdots & \mathbf{k}_{sH\,1n}\\ \vdots & \ddots & \vdots\\ \mathbf{k}_{sH\,n1} & \cdots & \mathbf{k}_{sH\,nn}\end{bmatrix} \tag{71}$$

Matrix $\mathbf{K}_s$ is a block diagonal matrix collecting the stiffness of all quadrature cross-sections, and $\mathbf{K}_{sH}$ accounts for the coupling due to the curvature and shear integration. The general sub-matrix $\mathbf{k}_{sH\,\alpha\beta}$ results as:

$$\mathbf{k}_{sH\,\alpha\beta} = p_{x\,j}\begin{bmatrix}0 & 0 & 0 & 0 & 0 & 0\\ 0 & \mathbf{H}_{\chi\,\alpha\beta} & \mathbf{H}_{\gamma\,\alpha\beta} & 0 & 0 & 0\\ 0 & -\mathbf{H}'_{\chi\,\alpha\beta} & -\mathbf{H}'_{\gamma\,\alpha\beta} & 0 & 0 & 0\\ 0 & 0 & 0 & 0 & 0 & 0\\ 0 & 0 & 0 & 0 & \mathbf{H}_{\chi\,\alpha\beta} & -\mathbf{H}_{\gamma\,\alpha\beta}\\ 0 & 0 & 0 & 0 & \mathbf{H}'_{\chi\,\alpha\beta} & -\mathbf{H}'_{\gamma\,\alpha\beta}\end{bmatrix} \tag{72}$$

being $\mathbf{H}_{\chi\,\alpha\beta}$, $\mathbf{H}'_{\chi\,\alpha\beta}$, $\mathbf{H}_{\gamma\,\alpha\beta}$ and $\mathbf{H}'_{\gamma\,\alpha\beta}$ the terms on the row α and column β of the matrices $\mathbf{H}_\chi$, $\mathbf{H}'_\chi$, $\mathbf{H}_\gamma$ and $\mathbf{H}'_\gamma$, respectively (Section 3).
A consistent non-iterative scheme [26] is obtained by setting to 1 the maximum number of internal iterations $I_{l\,max}$.

Appendix B. Fornberg algorithm for FD coefficient computation

Given a sufficiently smooth 1D function $f(\xi)$ and the values that this assumes at n abscissas $\xi_1, \xi_2, \ldots, \xi_n$, anyhow distributed along the domain, the Fornberg algorithm permits to compute the FD coefficients to approximate the derivative of $f(\xi)$ of any order. Specifically, the algorithm computes the FD coefficients to approximate all the derivatives, up to the order m_{max}, evaluated at the general abscissa ξ_0, not necessarily coinciding with one of the n abscissas where $f(\xi)$ is known, i.e.:

$$\left.\frac{d^m f(\xi)}{d\xi^m}\right|_{\xi=\xi_0} \approx \sum_{q=1}^n \delta_{0q}^m f(\xi_q) = \left\{\delta_{01}^m\quad\delta_{02}^m\quad\cdots\quad\delta_{0n}^m\right\}\begin{Bmatrix}f(\xi_1)\\ f(\xi_2)\\ \vdots\\ f(\xi_n)\end{Bmatrix}\qquad\text{for}\quad m = 0, \ldots, m_{max} \tag{73}$$

The recursive algorithm works as reported in Table 2. Specifically, this considers n FD schemes with increasing number of points, as shown by the first loop governed by the counter p. The pth scheme of the loop includes the first p abscissas of the set. For each of these schemes, the algorithm loops over the considered p abscissas (second loop with counter q), except the last one, and computes

Table 2
Fornberg algorithm.

Given	$m_{max}, \xi_0, \xi_1, \xi_2, \ldots, \xi_n$	
Set	$N = n - 1$	
Define	zero three dimensional matrix $\boldsymbol{\delta}$ with size $(n \times n \times m_{max} + 1)$ to store the coefficients	
Set	first term $_0\delta_0^0 = \boldsymbol{\delta}(1,1,1) = 1$ (only value required for the scheme with 1 point, i.e., $p = 1$)	
Set	dummy quantity $c_1 = 1$	

Loop	for $p = 2, \ldots, n$ [*over the schemes*]		
	Set	dummy quantity $c_2 = 1$	
	Loop	for $q = 1, \ldots, p-1$ [*over the abscissas of the scheme except last one*]	
		Set	dummy quantities $c_3 = \xi_p - \xi_q$ and $c_2 = c_2 c_3$
		Loop	for $m = 0, \ldots, min\{p-1; m_{max}\}$ [*over the derivative order*]
			Get $_{p-2}\delta_{q-1}^m = \boldsymbol{\delta}(p-1, q, m+1)$
			If $m = 0$
			Set $_{p-1}\delta_{q-1}^0 = \boldsymbol{\delta}(p, q, 1) = \frac{(\xi_p - \xi_0)}{c_3}\, _{p-2}\delta_{q-1}^0$
			Else ($m > 0$)
			Get $_{p-2}\delta_{q-1}^{m-1} = \boldsymbol{\delta}(p-1, q, m)$
			Set $_{p-1}\delta_{q-1}^m = \boldsymbol{\delta}(p, q, m+1) = \frac{(\xi_p - \xi_0)}{c_3}\, _{p-2}\delta_{q-1}^m - \frac{m}{c_3}\, _{p-2}\delta_{q-1}^{m-1}$
			End
		End	
	End		
	Loop	for $m = 0, \ldots, min\{p-1; m_{max}\}$ [*over the derivative order*]	
		Get $_{p-2}\delta_{p-2}^m = \boldsymbol{\delta}(p-1, p-1, m+1)$	
		If $m = 0$	
		Set $_{p-1}\delta_{p-1}^0 = \boldsymbol{\delta}(p, p, 1) = \frac{c_1}{c_2}\left[-(\xi_{p-1} - \xi_0)\, _{p-2}\delta_{p-2}^0\right]$	
		Else ($m > 0$)	
		Get $_{p-2}\delta_{p-2}^{m-1} = \boldsymbol{\delta}(p-1, p-1, m)$	
		Set $_{p-1}\delta_{p-1}^m = \boldsymbol{\delta}(p, p, m+1) = \frac{c_1}{c_2}\left[m\, _{p-2}\delta_{p-2}^{m-1} - (\xi_{p-1} - \xi_0)\, _{p-2}\delta_{p-2}^m\right]$	
		End	
	End		
	Update	dummy quantity $c_1 = c_2$	
End			

the coefficients for the approximation of all possible derivatives up to the order m_{max} (third loop with counter m). Finally, the coefficient for the last point of the scheme are computed (last loop with counter m, where $q = p$).

The coefficients are stored in a three-dimensional matrix $\boldsymbol{\delta}$ with size $(n \times n \times m_{max} + 1)$. Hence, the general coefficient $_p\delta_{0q}^m$ is computed for the p-point scheme (first dimension of $\boldsymbol{\delta}$) and associated to the abscissa q (second dimension of $\boldsymbol{\delta}$), to approximate the derivative of order m (third dimension of $\boldsymbol{\delta}$). For brevity, subscript 0 indicating that the derivatives are evaluated at ξ_0 is dropped in Table 2, i.e., the general coefficient is indicated as $_p\delta_q^m$.

To be noted is that a p-point scheme permits to approximate only the derivative up to the order $p - 1$. Thus, when $m_{max} > p - 1$, the algorithm stops at the derivative of order $p - 1$.

Appendix C. Supplementary material

This paper includes supplementary material which consists of Matlab scripts and functions to compute matrices $\mathbf{H}_\chi$, $\mathbf{H}_\chi'$, $\mathbf{H}_\gamma$ and $\mathbf{H}_\gamma'$ (Eqs. (21) and (22)) with the proposed FDDI technique. Three files are included:

- MAIN.m → This is the main script file for running the computation. After defining the cross-section abscissas, given in the vector X, and the FD scheme order to be used (variable p), it calls the function ComputeMatrices4FDDI.

- ComputeMatrices4FDDI.m → This file contains the function ComputeMatrices4FDDI that performs the actual computation of the matrices $\mathbf{H}_\chi$, $\mathbf{H}_\chi'$, $\mathbf{H}_\gamma$ and $\mathbf{H}_\gamma'$ for a given set of quadrature cross-section abscissas (vector X) and the chosen FD scheme order (variable p $\leq$ n).
  If p = 3, the FDDI3 is used (Section 3.4.1), by calling the function FDDI_3pnt.
  If p = 4, the FDDI4 is used (Section 3.4.2), by calling the function FDDI_4pnt.
  If p = 5, the FDDI5 is used (Section 3.4.3), by calling the function FDDI_5pnt.
  Functions FDDI_3pnt, FDDI_4pnt and FDDI_5pnt are included in the same file and call the function Fornberg.

- Fornberg.m → This file contains the function Fornberg that computes the FD coefficients required by the functions FDDI_3pnt, FDDI_4pnt and FDDI_5pnt, based on the Fornberg algorithm (Appendix B).

The reader can refer to the header of each Matlab file for a more detailed description.

Appendix D. Supplementary data

Supplementary material related to this article can be found online at https://doi.org/10.1016/j.cma.2024.117067.

References

[1] J. Simo, L. Vu-Quoc, A three-dimensional finite-strain rod model. Part II: Computational aspects, Comput. Methods Appl. Mech. Engrg. 58 (1) (1986) 79–116.

[2] E. Spacone, F.C. Filippou, F.F. Taucer, Fibre beam-column model for non-linear analysis of R/C frames: Part I. formulation, Earthq. Eng. Struct. Dyn. 25 (7) (1996) 711–726.

[3] W. Smolenski, Statically and kinematically exact nonlinear theory of rods and its numerical verification, Comput. Methods Appl. Mech. Engrg. 178 (1–2) (1999) 99–113.

[4] O. Soydas, A. Saritas, An accurate nonlinear 3d timoshenko beam element based on hu-washizu functional, Int. J. Mech. Sci. 74 (2013) 1–14.

[5] P. Di Re, D. Addessi, F. Filippou, Mixed 3D beam element with damage plasticity for the analysis of RC members under warping torsion, J. Struct. Eng. - ASCE 144 (6) (2018) 04018064.

[6] R. De Souza, Force-Based Finite Element for Large Displacement Inelastic Analysis of Frames (Ph.D. thesis), University of California, Berkeley, CA, United States, 2000.

[7] F. Auricchio, P. Carotenuto, A. Reali, On the geometrically exact beam model: a consistent, effective and simple derivation from three-dimensional finite-elasticity, Int. J. Solids Struct. 45 (17) (2008) 4766–4781.

[8] E. Reissner, On one-dimensional finite-strain beam theory: the plane problem, J. Appl. Math. Phys. (ZAMP) 23 (5) (1972) 795–804.

[9] T. Belytschko, L. Glaum, Applications of higher order corotational stretch theories to nonlinear finite element analysis, Comput. Struct. 10 (1–2) (1979) 175–182.

[10] J. Simo, A finite strain beam formulation. The three-dimensional dynamic problem. Part I, Comput. Methods Appl. Mech. Engrg. 49 (1) (1985) 55–70.

[11] R. Silveira, A. Galvão, P. Gonçalves, A comparative study of some non-linear formulations for the analysis of plane frames, in: European Congress on Computational Methods in Applied Sciences and Engineering, ECCOMAS 2000, 2000, pp. 1–20.

[12] M. Schulz, F. Filippou, Non-linear spatial Timoshenko beam element with curvature interpolation, Internat. J. Numer. Methods Engrg. 50 (4) (2001) 761–785.

[13] R. Alves, Non-Linear Elastic Instability of Space Frames (Ph.D. thesis), Federal University of Rio de Janeiro, UFRJ-COPPE 1995, (in Portuguese).

[14] Y.B. Yang, S.R. Kuo, Theory and Analysis of Nonlinear Framed Structures, Prentice Hall, 1994.

[15] C. Pacoste, A. Eriksson, Beam elements in instability problems, Comput. Methods Appl. Mech. Engrg. 144 (1–2) (1997) 163–197.

[16] S. Antman, Kirchhoff's problem for nonlinearly elastic rods, Q. Appl. Math. 32 (3) (1974) 221–240.

[17] E. Dvorkin, E. Oñate, J. Oliver, On a non-linear formulation for curved Timoshenko beam elements considering large displacement/rotation increments, Internat. J. Numer. Methods Engrg. 26 (7) (1988) 1597–1613.

[18] M. Jirasek, E. La Malfa Ribolla, M. Horak, Efficient finite difference formulation of a geometrically nonlinear beam element, Internat. J. Numer. Methods Engrg. 122 (23) (2021) 7013–7053.

[19] B. Nour-Omid, C.C. Rankin, Finite rotation analysis and consistent linearization using projectors, Comput. Methods Appl. Mech. Engrg. 93 (3) (1991) 353–384.

[20] M.A. Crisfield, G.F. Moita, A unified co-rotational for solids, shells and beams, Int. J. Solids Struct. 81 (20–22) (1996) 2969–2992.

[21] B. Izzuddin, A. Elnashai, Eulerian formulation for large-displacement analysis of space frames, J. Eng. Mech. 119 (3) (1993) 549–569.

[22] D. Addessi, P. Di Re, E. Sacco, Micromechanical and multiscale computational modeling for stability analysis of masonry elements, Eng. Struct. 211 (2020) 110428.

[23] C.A. Felippa, B. Haugen, A unified formulation of small-strain corotational finite elements: I. Theory, Comput. Methods Appl. Mech. Engrg. 194 (21) (2005) 2285–2335.

[24] J.M. Battini, C. Pacoste, Co-rotational beam elements with warping effects in instability problems, Comput. Methods Appl. Mech. Engrg. 191 (17) (2002) 1755–1789.

[25] J.M. Battini, A modified corotational framework for triangular shell elements, Comput. Methods Appl. Mech. Engrg. 196 (13) (2007) 1905–1914.

[26] A. Neuenhofer, F.C. Filippou, Evaluation of nonlinear frame finite-elementmodels, J. Struct. Eng. 123 (7) (1997) 958–966.

[27] M. Petrangeli, P.E. Pinto, V. Ciampi, Fiber element for cyclic bending and shear of rc structures. I: Theory, J. Eng. Mech. 125 (9) (1999) 994–1001.

[28] K. Hjelmstad, E. Taciroglu, Mixed methods and flexibility approaches for nonlinear frame analysis, J. Constr. Steel Res. 58 (5–8) (2002) 967–993.

[29] R.L. Taylor, F.C. Filippou, A. Saritas, F. Auricchio, A mixed finite element method for beam and frame problems, Comput. Mech. 31 (1–2) (2003) 192–203.

[30] M.H. Scott, G.L. Fenves, Plastic hinge integration methods for force-based beam-column elements, J. Struct. Eng. - ASCE 132 (2) (2006) 244–252.

[31] P. Di Re, D. Addessi, E. Sacco, A multiscale force-based curved beam element for masonry arches, Comput. Struct. 208 (2018) 17–31.

[32] D. Addessi, P. Di Re, G. Cimarello, Enriched beam finite element models with torsion and shear warping for the analysis of thin-walled structures, Thin-Walled Struct. 159 (2021) 107259.

[33] D. Magisano, L. Leonetti, A. Madeo, G. Garcea, A large rotation finite element analysis of 3D beams by incremental rotation vector and exact strain measure with all the desirable features, Comput. Methods Appl. Mech. Engrg. 361 (2020) 112811.

[34] A. Neuenhofer, F. Filippou, Geometrically nonlinear flexibility-based frame finite element, J. Struct. Eng. - ASCE 124 (6) (1998) 704–711.

[35] E. Sacco, A consistent model for first-order moderate rotation plate theory, Internat. J. Numer. Methods Engrg. 35 (10) (1992) 2049–2066.

[36] P. Khodabakhshi, J. Reddy, A unified beam theory with strain gradient effect and the von Kármán nonlinearity, ZAMM-J. Appl. Math. Mech. 97 (7) (2017) 70–91.

[37] M. Sivaselvan, A. Reinhorn, Collapse analysis: large inelastic deformations analysis of planar frames, J. Struct. Eng. - ASCE 128 (12) (2002) 1575–1583.

[38] D. Magisano, L. Leonetti, G. Garcea, Advantages of the mixed format in geometrically nonlinear analysis of beams and shells using solid finite elements, Internat. J. Numer. Methods Engrg. 109 (9) (2016) 1237–1262.

[39] D. Magisano, L. Leonetti, G. Garcea, Isogeometric analysis of 3D beams for arbitrarily large rotations: Locking-free and path-independent solution without displacement DOFs inside the patch, Comput. Methods Appl. Mech. Engrg. 373 (2021) 113437.

[40] D. Magisano, A. Corrado, New robust and efficient global iterations for large deformation finite element analysis of beams and shells with material nonlinearity, Comput. Methods Appl. Mech. Engrg. 406 (2023) 115900.

[41] V. Jafari, M. Abyaneh, S. Vahdani, M. Rahimian, Improved displacement-field approximation for geometrical nonlinear flexibility-based planar curved element in state space, Mech. Based Des. Struct. Mach. 37 (4) (2009) 475–502.

[42] V. Jafari, S. Vahdani, M. Rahimian, Derivation of the consistent flexibility matrix for geometrically nonlinear Timoshenko frame finite element, Finite Elem. Anal. Des. 46 (12) (2010) 1077–1085.

[43] M.H. Scott, V. Jafari Azad, Response sensitivity of material and geometric nonlinear force-based Timoshenko frame elements, Internat. J. Numer. Methods Engrg. 111 (5) (2017) 474–492.

[44] M. Rezaiee-Pajand, N. Gharaei-Moghaddam, Analysis of 3D Timoshenko frames having geometrical and material nonlinearities, Int. J. Mech. Sci. 94–95 (2015) 140–155.

[45] D. Feng, X. Chen, F. McKenna, E. Taciroglu, Consistent nonlocal integral and gradient formulations for force-based Timoshenko elements with material and geometric nonlinearities, J. Struct. Eng. - ASCE 149 (4) (2023) 04023018.

[46] M. Scott, M. Denavit, Generalized computation of buckling loads via curvature-based displacement interpolation, J. Struct. Eng. - ASCE 149 (2) (2023) 04022231.

[47] P. Di Re, D. Addessi, C. Gatta, L. Parente, E. Sacco, Corotational force-based beam finite element with rigid joint offsets for 3D framed structures, Comput. Methods Appl. Mech. Engrg. 419 (2024) 116656.

[48] P. Di Re, D. Addessi, A mixed 3D corotational beam with cross-section warping for the analysis of damaging structures under large displacements, Meccanica 53 (6) (2018) 1313–1332, http://dx.doi.org/10.1007/s11012-017-0749-3.

[49] V. Le Corvec, Nonlinear 3d Frame Element with Multi-Axial Coupling Under Consideration of Local Effects (Ph.D. thesis), University of California, Berkeley, CA, United States, 2012.

[50] S.S. Antman, The theory of rods, in: C. Truesdell (Ed.), in: Linear Theories of Elasticity and Thermoelasticity, Springer, Berlin, Heidelberg, 1972.

[51] M. Pignataro, A. Di Carlo, R. Casciaro, On nonlinear beam models from the point of view of computational post-buckling analysis, Int. J. Solids Struct. 18 (4) (1982) 327–347.

[52] Y. Pi, M. Bradford, B. Uy, A spatially curved-beam element with warping and Wagner effects, Internat. J. Numer. Methods Engrg. 63 (9) (2005) 1342–1369.

[53] D. Magisano, G. Garcea, Fiber-based shakedown analysis of three-dimensional frames under multiple load combinations: Mixed finite elements and incremental-iterative solution, Internat. J. Numer. Methods Engrg. 121 (17) (2020) 3743–3767.

[54] K. Bathe, Finite Element Procedures, Prentice Hall, Pearson Education Inc., 2006.

[55] G. Golub, C.F. Van Loan, Matrix Computations, second ed., Johns Hopkins, Baltimore, 1989.

[56] R.J. LeVeque, Finite Difference Methods for Ordinary and Partial Differential Equations: Steady-State and Time-Dependent Problems, Society for Industrial and Applied Mathematics, 2007.

[57] H. Langtangen, S. Linge, Finite Difference Computing with PDEs: a Modern Software Approach, Springer Nature, 2017.

[58] B. Cheong Khoo, J. White, J. Peraire, A. Patera, Lecture notes of the course "Numerical Methods For Partial Differential Equations (SMA 5212)", 2023, URL https://ocw.mit.edu/courses/16-920j-numerical-methods-for-partial-differential-equations-sma-5212-spring-2003/pages/lecture-notes/. (Online resource. Last access 23 July 2023).

[59] A. Saritas, F.C. Filippou, Inelastic axial-flexure-shear coupling in a mixed formulation beam finite element, Int. J. Non-Linear Mech. 44 (8) (2009) 913–922.

[60] B. Fornberg, Generation of finite difference formulas on arbitrarily spaced grids, Math. Comp. 51 (184) (1988) 699–706.

[61] R. MacAusland, The Moore-Penrose Inverse and Least Squares, University of Puget Sound. Math 420: Advanced Topics in Linear Algebra, 2014.

[62] G. Strang, Linear Algebra and Its Applications, Cengage India, 2012.

[63] S. Lee, F. Manuel, E. Rossow, Large deflections and stability of elastic frame, J. Eng. Mech. Div. 94 (2) (1968) 521–548.

[64] J. Argyris, B. Boni, U. Hindenlang, M. Kleiber, Finite element analysis of two-and three-dimensional elasto-plastic frames – The natural approach, Comput. Methods Appl. Mech. Engrg. 35 (2) (1982) 221–248.

[65] S.M. Kostic, F.C. Filippou, Section discretization of fiber beam-column elements for cyclic inelastic response, J. Struct. Eng. - ASCE 138 (5) (2012) 592–601.

[66] S. Kostic, F. Filippou, An adaptive section discretization scheme for the nonlinear dynamic analysis of steel frames, J. Struct. Eng. - ASCE 149 (4) (2023) 04023015.

[67] P. Di Re, D. Addessi, Computational enhancement of a mixed 3D beam finite element with warping and damage, J. Appl. Comput. Mech. 8 (1) (2022) 260–281.

[68] Z. Li, S. Cen, C. Wu, Y. Shang, C. Li, High-performance geometric nonlinear analysis with the unsymmetric 4-node, 8-DOF plane element US-ATFQ4, Internat. J. Numer. Methods Engrg. 114 (9) (2018) 931–954.

[69] C. Cichon, Large displacements in-plane analysis of elastic-plastic frames, Comput. Struct. 19 (1984) 737–745.

[70] R. Abbasnia, A. Kassimali, Large deformation elastic-plastic analysis of space frames, J. Constr. Steel Res. 35 (3) (1995) 275–290.